Distributed Cooperative Control of DC Microgrids

Vahidreza Nasirian, *Student Member, IEEE*, Seyedali Moayedi, *Student Member, IEEE*, Ali Davoudi, *Member, IEEE*, and Frank L. Lewis, *Fellow, IEEE*

***Abstract*—A cooperative control paradigm is used to establish a distributed secondary/primary control framework for dc microgrids. The conventional secondary control, that adjusts the voltage set point for the local droop mechanism, is replaced by a voltage regulator and a current regulator. A noise-resilient voltage observer is introduced that uses neighbors' data to estimate the average voltage across the microgrid. The voltage regulator processes this estimation and generates a voltage correction term to adjust the local voltage set point. This adjustment maintains the microgrid voltage level as desired by the tertiary control. The current regulator compares the local per-unit current of each converter with the neighbors' and, accordingly, provides a second voltage correction term to synchronize per-unit currents and, thus, provide proportional load sharing. The proposed controller precisely handles the transmission line impedances. The controller on each converter communicates with only its neighbor converters on a communication graph. The graph is a sparse network of communication links spanned across the microgrid to facilitate data exchange. The global dynamic model of the microgrid is derived, and design guidelines are provided to tune the system's dynamic response. A low-voltage dc microgrid prototype is set up, where the controller performance, noise resiliency, link-failure resiliency, and the plug-and-play capability features are successfully verified.**

***Index Terms*—Cooperative control, dc–dc converter, dc microgrid, distributed control, droop control.**

I. Introduction

ACTIVE distribution systems are moving toward a distributed structure [1]–[3]. Compared to the centralized generation, distributed generation offers improved efficiency [4], [5], reliability [6]–[9], expandability [10], and stability [11], [12]. Microgrids, as small-scale power systems where generation, consumption, and storage happen in a close physical vicinity, are becoming popular in distribution systems [13]–[15]. Although inverter-based ac microgrids have been prevalent, dc microgrid are currently emerging at distribution levels. The dc nature of emerging renewable energy sources (e.g., solar) or storage units (e.g., batteries and ultracapacitors) efficiently lends itself to a dc microgrid paradigm that avoids redundant conversion stages [5], [16]. Many of new loads are electronic dc loads (e.g., in data centers). Even some traditional ac loads, e.g., induction machines, can appear as dc loads when controlled by inverter-fed drive systems [17]. DC microgrids are also shown to have about two orders-of-magnitude more availability compared to their ac counterparts, thus making them ideal candidates for mission-critical applications [7], [18]. Moreover, dc microgrids can overcome some disadvantages of ac systems, e.g., transformer inrush current, frequency synchronization, reactive power flow, power quality issues, etc. [19].

Resembling the control hierarchy of the legacy grid, a hierarchical control structure is conventionally adopted for microgrid operation [1], [20]. The highest hierarchy, the tertiary control, is in charge of economical operation and coordination with the distribution system operator. It assigns the microgrid voltage to carry out the scheduled power exchange between the microgrid and the main grid [21]–[24]. To satisfy the voltage demand of the tertiary control, the secondary control measures voltages across the microgrid and, accordingly, updates the voltage set points for the primary controllers. The primary control, typically implemented locally with a droop mechanism, regulates the output voltage of individual converters.

The secondary and tertiary controls are typically implemented in a centralized fashion [25], [26], which communicates with converters through communication links with high connectivity. Loss of any link in such a topology can lead to the failure of the corresponding unit and, thus, overstressing other units, leading to system-level instability and cascaded failures [27]. Since future extensions add to the complexity of the controller, scalability of central controllers is not straightforward. Distributed control has emerged as an attractive alternative as it offers improved reliability, simpler communication network, and easier scalability [26]. For example, distributed tertiary control via dc bus signaling is studied in [28]–[30]. Structurally, it is desired to extend the distributed control paradigm to the secondary/primary controls. Categorically, such a controller shall satisfy two main control objectives of dc microgrids, namely voltage regulation [31] and proportional load sharing [32].

Proper load sharing assigns the load among participating converters in proportion to their rated power. This equalizes the per-unit currents of all sources, and prevents circulating currents [32] and overstressing of any source [10], [33]–[35]. The droop control is widely adopted for load sharing by imposing virtual output impedance on each converter [35]–[37]. Static/dynamic performance and stability assessment of droop controllers are investigated in [38]–[42]. Despite simplicity and ease of implementation, the conventional droop method suffers from poor voltage regulation and load sharing, particularly when the line impedances are not negligible [43]–[46]. The primary reason for this poor voltage regulation is the voltage drop caused by the virtual impedance. Another factor is the output voltage mismatch among different converters, which is crucial for the natural power flow in dc systems but further exacerbates the voltage regulation issue.

Manuscript received December 12, 2013; revised April 7, 2014; accepted April 30, 2014. Date of publication May 16, 2014; date of current version November 3, 2014. This work was supported in part by the National Science Foundation under grants ECCS-1137354 and ECCS-1128050 and the UT-Transform program. Recommended for publication by Associate Editor J. M. Guerrero.

The authors are with the Department of Electrical Engineering, University of Texas at Arlington, Arlington, TX 76019 USA (e-mail: vahidreza.nasirian@mavs.uta.edu; seyedali.moayedi@mavs.uta.edu; davoudi@uta.edu; lewis@uta.edu).

Color versions of one or more of the figures in this paper are available online at http://ieeexplore.ieee.org.

Digital Object Identifier 10.1109/TPEL.2014.2324579

Possible solutions to the aforementioned issues have been reviewed in [26]. These solutions are either centralized [1] or require establishment of a fully connected communication network throughout the microgrid, where any two nodes are directly connected [36], [47]–[49]. For example, a centralized secondary control in [1] measures the microgrid voltage, calculates a voltage restoration term, and sends the restoration term to all sources. It assumes equal voltages for all converters across the microgrid, which is not a viable assumption for dc microgrids. Adaptive droop control in [50] and [51] further improves performance, but the line impedance is neglected. High droop gains in [26] mitigate power-sharing discrepancy caused by the line impedances. In [52], a communication network is spread all over the microgrid and the functionality of the centralized secondary controller is embedded in each converter. Point-to-point communication links are required for all sources and any link failure renders the whole microgrid inoperable. The line impedance effect is taken into account in [43], with a fully connected communication network. Despite improved accuracy, systems with a fully connected communication network are susceptible to failure as any link failure impairs the whole control functionality. Future extension is another challenge; after any structural/electrical upgrade, some control settings, e.g., the number of sources, need to be updated and embedded in all converters. The voltage regulation requirement is redefined to incorporate the line impedance effect in [43] and [53]. Accordingly, it is required that the average voltage across the microgrid (and only not a specific bus voltage) is regulated at the global voltage set point determined by the tertiary control. This is called the *global voltage regulation*, and is considered here.

This paper focuses on the secondary/primary control of the dc microgrids. The salient features of the proposed distributed cooperative control are as follows.

1) Cooperation among converters on a communication graph is used to provide additional correction terms and fine tune the local voltage set point for each converter.
2) Each converter is augmented with a voltage regulator. This regulator uses the estimation made by the voltage observer to adjust the local voltage set point and provide global voltage regulation.
3) A current regulator is also added that compares the actual per-unit current of a converter with a weighted average of its neighbors' and, accordingly, generates a voltage correction term to provide proportional load sharing.
4) Cooperation of the voltage and current regulators is shown to effectively carry out both global voltage regulation and proportional load sharing, particularly, when the line impedances are not negligible.
5) A noise-resilient voltage observer is introduced that processes both local and neighbors' voltage approximation to estimate the global average voltage across the microgrid.
6) The control scheme does not require *a priori* knowledge of the global parameters such as the number of sources. Thus, it is scalable and features the plug-and-play capability.
7) A sparse communication network is spanned across the microgrid that enables limited message passing among converters; each converter only exchanges data with its neighbors. This is in direct contrast to the centralized control approaches which require communication networks with high-bandwidth communication links and a high level of connectivity.

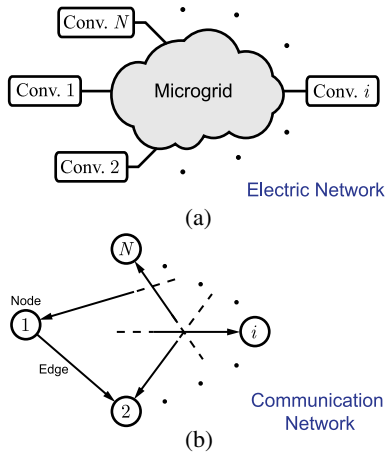

Fig. 1. General layout of a dc Microgrid. (a) Converters supplying the grid. (b) Communication network spanned among sources for data exchange.

The rest of this paper is outlined as follows. Section II is a preliminary review of graph theory. The proposed cooperative control paradigm is discussed in Section III. The voltage observer is introduced in Section IV. Section V studies the global dynamic/static model of the microgrid and tuning of the proposed controller. The controller performance is verified using a low-voltage dc microgrid prototype in Section VI. Section VII concludes the paper.

II. Preliminary Review of Graph Theory

Fig. 1 shows the mapping of a cyber network to a physical microgrid. The nodes represent converters and edges represent communication links for data exchange. The communication graph does not need to have the same topology as the underlying physical microgrid. This cyber connection lays the ground work for the cooperative control paradigm, where neighbors' interactions can lead to a global consensus. Accordingly, not all agents (converters) in a large-scale dynamic system need to be in a direct contact. Instead, each agent only exchanges control variables with its neighbors. Then, using the neighbors' data and its local measurements, the agent updates its control variables. The cooperative control offers global consensus of the desired variables, provided that the communication graph is properly designed.

Fig. 1(b) shows a directed graph (digraph) associated with the cyber layer connecting the microgrid converters in Fig. 1(a). Such a graph is usually represented as a set of nodes $\mathbf{V_G} = \{v_1^g, v_2^g, \ldots, v_N^g\}$ connected through a set of edges $\mathbf{E_G} \subset \mathbf{V_G} \times \mathbf{V_G}$, and an associated adjacency matrix $\mathbf{A_G} = [a_{ij}] \in \mathbb{R}^{N\times N}$. N is the number of nodes. The adjacency matrix $\mathbf{A_G}$ contains the communication weights, where $a_{ij} > 0$ if $(v_j^g, v_i^g) \in \mathbf{E_G}$ and $a_{ij} = 0$, otherwise. a_{ij} is the communication weight for data transfer from node j to node

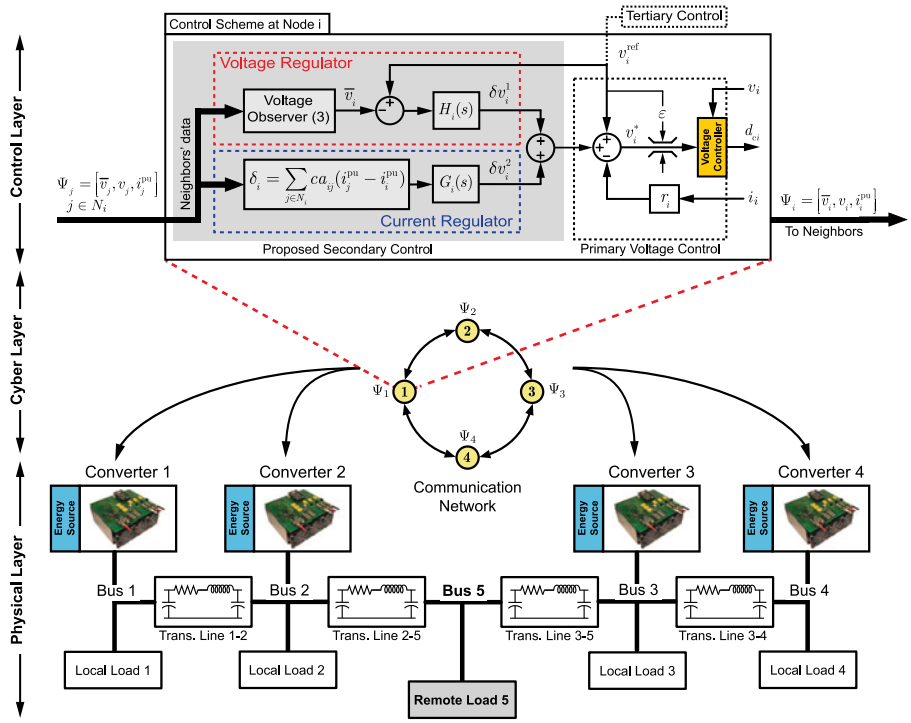

Fig. 2. Proposed distributed cooperative control for dc microgrids.

i. Here, the adjacency matrix is assumed to be time invariant. $N_i = \{j | (v_j^{\rm g}, v_i^{\rm g}) \in \mathbf{E_G}\}$ denotes the set of all neighbors of node i, i.e., if $j \in N_i$, then $v_i^{\rm g}$ receives information from $v_j^{\rm g}$. However, in a digraph, the link is not necessarily reciprocal, i.e., $v_j^{\rm g}$ might not receive information from $v_i^{\rm g}$. The in-degree matrix $\mathbf{D}_{\mathbf{G}}^{\rm in} = {\rm diag}\{d_i^{\rm in}\}$ is a diagonal matrix with $d_i^{\rm in} = \sum_{j \in N_i} a_{ij}$. Similarly, the out-degree matrix is $\mathbf{D}_{\mathbf{G}}^{\rm out} = {\rm diag}\{d_i^{\rm out}\}$, where $d_i^{\rm out} = \sum_{i \in N_j} a_{ji}$. The Laplacian matrix is defined as $\mathbf{L} = \mathbf{D}_{\mathbf{G}}^{\rm in} - \mathbf{A_G}$, whose eigenvalues determine the global dynamics [54]. The Laplacian matrix is balanced if the in-degree of each node matches its out-degree, i.e., $\mathbf{D}_{\mathbf{G}}^{\rm in} = \mathbf{D}_{\mathbf{G}}^{\rm out}$. In particular, if the graph is undirected, i.e., all links are bidirectional then, the Laplacian matrix is balanced. A direct path from $v_i^{\rm g}$ to $v_j^{\rm g}$ is a sequence of edges that connects the two nodes. A digraph is said to have a spanning tree if it contains a root node, from which there exists at least a direct path to every other node.

III. Cooperative Secondary Control

Fig. 2 shows the layout of a typical dc microgrid, where the physical, cyber, and control layers are illustrated. The physical layer consists of the dispatchable sources (including the power electronics converters), transmission lines, and loads. A cyber layer, comprised of all communication links, is spanned among the sources to facilitate data exchange. This is a sparse communication network with at least a spanning tree and is also chosen such that in case of any link failure the remaining network still contains a spanning tree. Although the graph illustrated in Fig. 2 is undirected (bidirectional), directed graphs can be used in a general case. Each converter transmits a set of data, $\Psi_i = [\bar{v}_i, v_i, i_i^{\rm pu}]$, to its neighbors. The dataset transmitted by node i, Ψ_i consists of three elements; its estimate of the average voltage across the microgrid $\bar{v}_i$, the measured local voltage v_i, and the measured per-unit current $i_i^{\rm pu}$. The per-unit term here refers to the current provided by the converter divided by its rated current, i.e., $i_i^{\rm pu} \triangleq i_i / I_i^{\rm rated}$, where $I_i^{\rm rated}$ is the rated current of the ith converter. Thus, individual converters may use different values as their base currents (i.e., their rated currents), unlike the conventional per-unit terminology, where converters in the same voltage zone share identical values for base currents. This terminology of the per-unit current is used here to represent loading percentage of each converter. At the other end of the communication links, each converter j receives data from all its neighbors $\Psi_k,\ k \in N_j$ with communication weights a_{jk}. These communication weights are design parameters and can be considered as data transfer gains.

The global voltage regulation and proportional load sharing are the two objectives of the secondary/primary control, which require proper voltage set point assignment for the individual converters. The proposed secondary controller is highlighted in Fig. 2, where local and neighbors' information are processed to adjust the local voltage set point v_i^*. The starting point is the conventional droop mechanism that characterizes the converter output impedance using a virtual impedance r_i. The droop controller, at a primary control level, acts on local information. When operating conditions vary, the droop mechanism promptly initiates the voltage adjustment. However, this local control has a limited performance. Cooperation among converters, at the secondary control level, can help properly fine-tune the voltage set points v_i^* and mitigate the current and voltage residuals.

The voltage set point for the droop control is augmented with two correction terms. These correction terms are provided through cooperation among converters. They are resulted from voltage and current regulators that help fine adjustment of the local voltage set points, i.e., v_i^* s to provide global voltage regulation and proportional load sharing. Based on Fig. 2, the local voltage set point for an individual converter can be expressed as

$$v_i^* = v_i^{\rm ref} - r_i i_i + \delta v_i^1 + \delta v_i^2. \tag{1}$$

This set point is further adjusted by a voltage limiter (see Fig. 2) to maintain the bus voltages within an acceptable range.

The voltage regulator consists of a voltage observer and a PI controller H_i. The voltage observer at each node estimates the averaged voltage across the microgrid, where $\bar{v}_i$ is the estimation at node i. This estimation is then compared with the global reference voltage $v_i^{\rm ref}$ to generate the first voltage correction term δv_i^1. In case of any mismatch between $\bar{v}_i$ and $v_i^{\rm ref}$, the controller adjusts δv_i^1 to eliminate the discrepancy. In the islanded mode of operation, the global reference voltage $v_i^{\rm ref}$ are typically all equal to the rated voltage of the microgrid. However, in the grid-connected mode, where the microgrid exchanges power with the main grid, the tertiary control sets a new voltage level for the microgrid and relays the new reference value to individual converters. A cooperative observer will process the local voltage measurement and the neighbors' estimates to evaluate the average voltage across the microgrid. Functionality of the observer is discussed in detail in Section IV. The line impedances might incapacitate the droop mechanism to proportionally share the load. Herein, a cooperative current regulator generates the second voltage correction term δv_i^2. The regulator at node i compares the local per-unit current $i_i^{\rm pu}$ with a weighted averaged of the neighbors' per-unit currents to find the current mismatch δ_i

$$\delta_i = \sum_{j\in N_i} c a_{ij}(i_j^{\rm pu} - i_i^{\rm pu}) \tag{2}$$

where c is the coupling gain between the voltage and current regulators. The current mismatch δ_i is fed to a PI controller G_i, which calculates the second voltage correction term δv_i^2. If the per-unit currents of any two neighbors' differ, the current regulators of the corresponding converters respond and adjust their second voltage correction terms to gain balance.

The current regulator itself (without the droop mechanism shown in Fig. 2) can accurately carry out the proportional load sharing. The droop mechanism, however, is typically a part of the primary controller and might be already embedded with the power electronic converter without any deactivation flexibility. Therefore, it is included in the primary controller of Fig. 2 to show that the current regulator can handle the load sharing even in the presence of the droop mechanism.

The primary voltage controller typically includes a voltage limiter (see Fig. 2). These limiters carry out two tasks: they limit voltage variations at the source terminals and also limit transmission line loading. According to Fig. 2, each output voltage is limited to $v_i^{\rm ref} - \varepsilon \le v_i \le v_i^{\rm ref} + \varepsilon$. With no loss of generality, one can assume that all converters use identical reference voltages, i.e., $v_i^{\rm ref} = v_{\rm ref}$ for all $1 \le i \le N$. Accordingly, voltage difference between every two nodes does not exceed the voltage limit band, i.e., $|v_i - v_j| \le 2\varepsilon$. Equivalently, the transmission line current will be limited to $i_{ij} \le 2\varepsilon/r_{ij}$, where r_{ij} is the series resistance of the transmission line between nodes i and j.

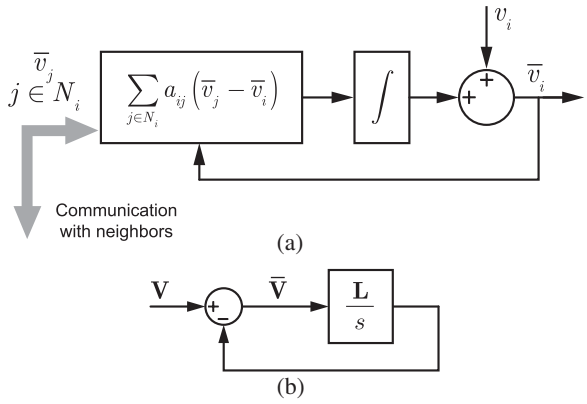

Fig. 3. Dynamic consensus protocol. (a) Averaging policy at each node. (b) Global model of the averaging technique in the frequency domain.

IV. Voltage Observer

The observer module is a part of the voltage regulator module, as shown in Fig. 2. It uses a dynamic cooperative framework to process neighbors' information and estimate the average voltage across the microgrid.

A. Dynamic Consensus

Fig. 3(a) shows the cooperative distributed approach for the global averaging. The observer at node i receives its neighbors' estimates $\bar{v}_j$ s ($j \in N_i$). Then, the observer updates its own estimate $\bar{v}_i$ by processing the neighbors' estimates and the local voltage measurement v_i

$$\bar{v}_i(t) = v_i(t) + \int_0^t \sum_{j\in N_i} a_{ij}\left(\bar{v}_j(\tau) - \bar{v}_i(\tau)\right) {\rm d}\tau. \tag{3}$$

This updating protocol is commonly referred to as *dynamic consensus* in the literature [55]. As seen in (3), the local measurement, e.g., v_i, is directly fed into the estimation protocol. Thus, in case of any voltage variation at node i, the local estimate $\bar{v}_i$ immediately responds. Then, the change in $\bar{v}_i$ propagates through the communication network and affects all other estimations. By differentiating (3)

$$\dot{\bar{v}}_i = \dot{v}_i + \sum_{j\in N_i} a_{ij}\left(\bar{v}_j - \bar{v}_i\right) = \dot{v}_i + \sum_{j\in N_i} a_{ij}\bar{v}_j - d_i^{\rm in}\bar{v}_i. \tag{4}$$

Accordingly, one can formulate the global observer dynamic as

$$\dot{\bar{\mathbf{v}}} = \dot{\mathbf{v}} + \mathbf{A_G}\bar{\mathbf{v}} - \mathbf{D_G^{in}}\bar{\mathbf{v}} = \dot{\mathbf{v}} - \left(\mathbf{D_G^{in}} - \mathbf{A_G}\right)\bar{\mathbf{v}} = \dot{\mathbf{v}} - \mathbf{L}\bar{\mathbf{v}} \tag{5}$$

where $\mathbf{v} = [v_1, v_2, \ldots, v_N]^{\rm T}$ is the voltage measurement vector, which carries measured voltage of all nodes. Also, $\bar{\mathbf{v}} = [\bar{v}_1, \bar{v}_2, \ldots, \bar{v}_N]^{\rm T}$ denotes the voltage estimation vector, which contains the global average voltage estimated by all

nodes. Equivalently, in the frequency domain

$$s\bar{\mathbf{V}} - \bar{\mathbf{v}}(0) = s\mathbf{V} - \mathbf{v}(0) - \mathbf{L}\bar{\mathbf{V}} \tag{6}$$

where $\mathbf{V}$ and $\bar{\mathbf{V}}$ are the Laplace transforms of $\mathbf{v}$ and $\bar{\mathbf{v}}$, respectively. Equation (3) implies that $\mathbf{v}(0) = \bar{\mathbf{v}}(0)$. Therefore

$$\bar{\mathbf{V}} = s(s\mathbf{I}_N + \mathbf{L})^{-1}\mathbf{V} = \mathbf{H}_{\text{obs}}\mathbf{V} \tag{7}$$

where $\mathbf{I}_N \in \mathbb{R}^{N\times N}$ and $\mathbf{H}_{\text{obs}}$ are the identity matrix and the observer transfer function, respectively. Equation (7) expresses the global dynamics of the voltage observers, whose block diagram is represented in Fig. 3(b). It is shown in the Appendix I that if $\mathbf{L}$ is balanced, then all elements of $\bar{\mathbf{v}}$ converge to a consensus value, which is the true average voltage, i.e., the average of all elements in $\mathbf{v}$. In other words

$$\bar{\mathbf{v}}^{\text{ss}} = \lim_{t\to\infty}\bar{\mathbf{v}}(t) = \mathbf{Q}\times\lim_{t\to\infty}\mathbf{v}(t) = \mathbf{Q}\mathbf{v}^{\text{ss}} = \langle\mathbf{v}^{\text{ss}}\rangle\,\underline{\mathbf{1}} \tag{8}$$

where $\mathbf{Q}\in\mathbb{R}^{N\times N}$ is the averaging matrix, whose elements are all equal to $1/N$. $\mathbf{x}^{\text{ss}}$ expresses the steady-state value of the vector $\mathbf{x}\in\mathbb{R}^{N\times 1}$. $\langle\mathbf{x}\rangle$ represents the average of all elements in the vector $\mathbf{x}$. $\underline{\mathbf{1}}\in\mathbb{R}^{N\times 1}$ is a vector whose elements are all equal to one.

B. Noise Cancellation Module

Disturbances may degrade the efficacy and accuracy of the voltage observers. Nonzero initial value of the integrator in Fig. 3(a) or read/write errors in digital storage devices are common disturbance sources in digital processing [56], [57]. For example, a nonzero initial value of any observer's integrator yields to an identical dc error in all estimations. Therefore, a noise cancellation module is essential to identify and cancel such disturbance/noises. Fig. 4(a) shows the proposed noise cancellation (NC) module incorporated in the voltage observer. A disturbance source d_i, highlighted in red, is assumed for the observer at node i. This source represents the aggregated effect of all possible disturbance/noises. The primary stage of the NC module is an observer, similar to that of Fig. 3(a), that estimates average of the voltage deviations w_i s, where $w_i = \bar{v}_i - v_i$. This stage is followed by an integrator to ensure disturbance tracking for dc and exponentially damping disturbances, e.g., a nonzero initial value for any integrator.

At each node, the NC module estimates $\langle\mathbf{w}\rangle$ as a noise indicator, where $\mathbf{w} = [w_1, w_2, \ldots, w_N]^{\text{T}}$ is the voltage deviation vector. If the noise cancellation term $\hat{d}_i$ is disabled for all nodes, with no noise corrupting the signals, i.e., $d_i = 0$ for all nodes, the voltage observers converge to the true average voltage. Thus

$$\mathbf{w} = \bar{\mathbf{v}} - \mathbf{v} \Rightarrow \langle\mathbf{w}^{\text{ss}}\rangle = \langle\bar{\mathbf{v}}^{\text{ss}}\rangle - \langle\mathbf{v}^{\text{ss}}\rangle = \mathbf{0}. \tag{9}$$

However, if any noise pollutes any observation, the voltage observations no longer converge to the global average, i.e., $\langle\bar{\mathbf{v}}^{\text{ss}}\rangle \neq \langle\mathbf{v}^{\text{ss}}\rangle$. Accordingly, $\langle\mathbf{w}^{\text{ss}}\rangle \neq \mathbf{0}$. Thus, $\langle\mathbf{w}\rangle$ is a suitable noise indicator. Accordingly, with activated NC module, it estimates $\langle\mathbf{w}\rangle$ and feeds the result into the integrator. If $\langle\mathbf{w}\rangle \neq \mathbf{0}$, the integrator adjusts the noise cancellation term $\hat{d}_i$, until it matches the noise, i.e., $\hat{d}_i = d_i$, and cancels its effect on the voltage estimations.

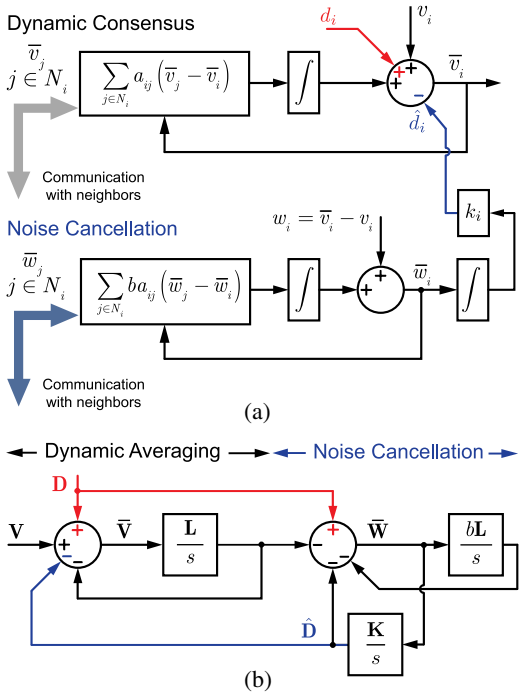

Fig. 4. Proposed dynamic consensus protocol with noise cancellation. (a) Averaging and noise cancellation policies at each node. (b) Global model of the averaging technique in the frequency domain.

Similar to (5), the total voltage observer dynamics can be derived by analyzing the policy explained in Fig. 4(a). Herein, the total observer is referred to as the observer in Fig. 4(a), which incorporates the NC module. According to this figure

$$\dot{\bar{\mathbf{v}}} = -\mathbf{L}\bar{\mathbf{v}} + \dot{\mathbf{v}} + \dot{\mathbf{d}} - \dot{\hat{\mathbf{d}}} \tag{10}$$

$$\dot{\hat{\mathbf{d}}} = \mathbf{K}\bar{\mathbf{w}} \tag{11}$$

$$\dot{\bar{\mathbf{w}}} = -b\mathbf{L}\bar{\mathbf{w}} + \dot{\mathbf{w}} = -b\mathbf{L}\bar{\mathbf{w}} + \dot{\bar{\mathbf{v}}} - \dot{\mathbf{v}} \tag{12}$$

where $\mathbf{d} = [d_1, d_2, \ldots, d_N]^{\text{T}}$ and $\hat{\mathbf{d}} = \left[\hat{d}_1, \hat{d}_2, \ldots, \hat{d}_N\right]^{\text{T}}$ are the actual and estimated disturbance vectors, respectively. $\bar{\mathbf{w}} = [\bar{w}_1, \bar{w}_2, \ldots, \bar{w}_N]^{\text{T}}$ is the estimated voltage deviation vector, $\mathbf{K} = \text{diag}\{k_i\}$ is the NC integrator gain matrix, b is the coupling gain between the main observer and the NC module. Equivalently, in the frequency domain

$$\begin{aligned}(s\mathbf{I}_N + \mathbf{L})\,\bar{\mathbf{V}} - \bar{\mathbf{v}}(0) = s\mathbf{V} - \mathbf{v}(0) + s\mathbf{D} - \mathbf{d}(0)\\ - s\hat{\mathbf{D}} + \hat{\mathbf{d}}(0)\end{aligned} \tag{13}$$

$$s\hat{\mathbf{D}} - \hat{\mathbf{d}}(0) = \mathbf{K}\bar{\mathbf{W}} \tag{14}$$

$$(s\mathbf{I}_N + b\mathbf{L})\,\bar{\mathbf{W}} - \bar{\mathbf{w}}(0) = s\bar{\mathbf{V}} - \bar{\mathbf{v}}(0) - s\mathbf{V} + \mathbf{v}(0) \tag{15}$$

where $\mathbf{D}$, $\hat{\mathbf{D}}$, and $\bar{\mathbf{W}}$ are the Laplace transforms of $\mathbf{d}$, $\hat{\mathbf{d}}$, and $\bar{\mathbf{w}}$, respectively. The initial conditions of the vectors involved in the total observer can be determined using Fig. 4(a). Accordingly

$$\hat{\mathbf{d}}(0) = \mathbf{0}, \quad \bar{\mathbf{v}}(0) = \mathbf{v}(0) + \mathbf{d}(0) \tag{16}$$

$$\bar{\mathbf{w}}(0) = \bar{\mathbf{v}}(0) - \mathbf{v}(0) = \mathbf{d}(0). \tag{17}$$

Each disturbance source d_i represents the aggregated effect of all possible disturbances at the corresponding node. Thus, the initial conditions of all the integrators in Fig. 4(a) can be safely assumed zero. Based on (13)–(17), the global block diagram of the total observer is shown in Fig. 4(b). One can simplify (13)–(15) using (16)–(17)

$$(s\mathbf{I}_N + \mathbf{L})\,\bar{\mathbf{V}} = s\mathbf{V} + s\mathbf{D} - \mathbf{K}\bar{\mathbf{W}} \tag{18}$$

$$(s\mathbf{I}_N + b\mathbf{L})\,\bar{\mathbf{W}} = s(\bar{\mathbf{V}} - \mathbf{V}). \tag{19}$$

Therefore

$$\left((s\mathbf{I}_N + \mathbf{L}) + s\mathbf{K}\,(s\mathbf{I}_N + b\mathbf{L})^{-1}\right)\bar{\mathbf{V}} = \left(s\mathbf{I}_N + s\mathbf{K}\,(s\mathbf{I}_N + b\mathbf{L})^{-1}\right)\mathbf{V} + s\mathbf{D} \tag{20}$$

which can be written as

$$\bar{\mathbf{V}} = \mathbf{H}^{\mathrm{F}}_{\mathrm{obs}}\mathbf{V} + \mathbf{H}_{\mathrm{NC}}\mathbf{D} \tag{21}$$

$$\mathbf{H}^{\mathrm{F}}_{\mathrm{obs}} = \left((s\mathbf{I}_N + \mathbf{L}) + s\mathbf{K}\,(s\mathbf{I}_N + b\mathbf{L})^{-1}\right)^{-1} \times \left(s\mathbf{I}_N + s\mathbf{K}\,(s\mathbf{I}_N + b\mathbf{L})^{-1}\right) \tag{22}$$

$$\mathbf{H}_{\mathrm{NC}} = s\left((s\mathbf{I}_N + \mathbf{L}) + s\mathbf{K}\,(s\mathbf{I}_N + b\mathbf{L})^{-1}\right)^{-1} \tag{23}$$

where $\mathbf{H}^{\mathrm{F}}_{\mathrm{obs}}$ and $\mathbf{H}_{\mathrm{NC}}$ are the total observer and NC transfer functions, respectively. It should be noted that for $\mathbf{K} = \mathbf{0}$, (22) and (7) provide the same functions. Basically, (7) presents the observer transfer function with a disabled NC module, where (22) expresses the function with an activated NC module. Appendix II shows that $\lim_{s\to 0}\mathbf{H}^{\mathrm{F}}_{\mathrm{obs}} = \mathbf{Q}$, which guarantees convergence of all estimations to the global average voltage. It should also be noted that $\mathbf{H}_{\mathrm{NC}}$ has a zero at the origin and, thus, for dc and exponentially damping disturbances, the second term in (21) decays to zero. Accordingly, the noise cancellation module successfully cancels any dc disturbance and attenuates any other disturbance according to its fundamental frequency. This is a satisfactory performance since most common disturbance sources in digital signal processing, such as nonzero integrator initial condition and read/write errors, have a dc or very low frequency nature [57].

V. Global Model Development

A. Global Dynamic Model

Let $\mathbf{v}_{\mathrm{ref}} = [v_1^{\mathrm{ref}}, v_2^{\mathrm{ref}}, \ldots, v_N^{\mathrm{ref}}]^{\mathrm{T}}$ and $\mathbf{i} = [i_1, i_2, \ldots, i_N]^{\mathrm{T}}$ be the global reference voltage and the actual supplied current vectors, respectively. $\mathbf{V}_{\mathrm{ref}}$ and $\mathbf{I}$ are the Laplace transforms of $\mathbf{v}_{\mathrm{ref}}$ and $\mathbf{i}$, respectively. Systematically, $\mathbf{V}_{\mathrm{ref}}$ is the input to the entire microgrid, where $\mathbf{V}$ and $\mathbf{I}$ are the outputs. A global dynamic model formulates the transfer functions from the input $\mathbf{V}_{\mathrm{ref}}$ to any outputs $\mathbf{V}$ and $\mathbf{I}$.

The cooperative distributed control of Fig. 2 introduces two voltage correction terms at each node δv_i^1 and δv_i^2. Accordingly

$$\Delta\mathbf{V}^1 = \mathbf{H}\left(\mathbf{V}_{\mathrm{ref}} - \bar{\mathbf{V}}\right) \tag{24}$$

$$\Delta\mathbf{V}^2 = -c\mathbf{G}\mathbf{L}\mathbf{I}^{\mathrm{pu}}. \tag{25}$$

$\Delta\mathbf{v}^1 = [\delta v_1^1, \delta v_2^1, \ldots, \delta v_N^1]^{\mathrm{T}}$ and $\Delta\mathbf{v}^2 = [\delta v_1^2, \delta v_2^2, \ldots, \delta v_N^2]^{\mathrm{T}}$ are the first and the second voltage correction vectors, respectively. $\Delta\mathbf{V}^1$ and $\Delta\mathbf{V}^2$ are the Laplace transforms of $\Delta\mathbf{v}^1$ and $\Delta\mathbf{v}^2$, respectively. $\mathbf{H} = \mathrm{diag}\{H_i\}$ and $\mathbf{G} = \mathrm{diag}\{G_i\}$ are the voltage and current controller matrices, respectively. $\mathbf{i}^{\mathrm{pu}} = [i_1^{\mathrm{pu}}, i_2^{\mathrm{pu}}, \ldots, i_N^{\mathrm{pu}}]^{\mathrm{T}}$ is the per-unit current vector with the Laplace transform of $\mathbf{I}^{\mathrm{pu}}$. One can write

$$\mathbf{I}^{\mathrm{pu}} = \mathbf{I}^{-1}_{\mathrm{rated}}\mathbf{I} \tag{26}$$

where $\mathbf{I}_{\mathrm{rated}} = \mathrm{diag}\{I_i^{\mathrm{rated}}\}$ and I_i^{rated} are the current rating matrix and the current rating of the converter at node i, respectively. Thus, by substituting (26) in (25)

$$\Delta\mathbf{V}^2 = -c\mathbf{G}\mathbf{L}\mathbf{I}^{-1}_{\mathrm{rated}}\mathbf{I}. \tag{27}$$

Let $\mathbf{v}^* = [v_1^*, v_2^*, \ldots, v_N^*]^{\mathrm{T}}$ be the vector of local voltage set points with the Laplace transform of $\mathbf{V}^*$. The proposed controller finds the local voltage set points according to

$$\mathbf{V}^* = \mathbf{V}_{\mathrm{ref}} + \Delta\mathbf{V}^1 + \Delta\mathbf{V}^2 - \mathbf{r}\mathbf{I} \tag{28}$$

where $\mathbf{r} = \mathrm{diag}\{r_i\}$ is the virtual impedance matrix. By substituting (24) and (27) in (28)

$$\mathbf{V}^* = (\mathbf{I}_N + \mathbf{H})\,\mathbf{V}_{\mathrm{ref}} - \mathbf{H}\bar{\mathbf{V}} - \left(c\mathbf{G}\mathbf{L}\mathbf{I}^{-1}_{\mathrm{rated}} + \mathbf{r}\right)\mathbf{I}. \tag{29}$$

On the other hand, dynamic behavior of any converter with a closed-loop voltage regulator can be modeled as

$$V_i = G_i^{\mathrm{c}}(s)V_i^* \tag{30}$$

where V_i and V_i^* are the Laplace transforms of v_i and v_i^*, respectively. G_i^{c} is the closed-loop transfer function of the converter at node i. The closed-loop transfer functions are formulated in [58] and [59] for a wide variety of converters. Global dynamic of the converters can be found as

$$\mathbf{V} = \mathbf{G}_{\mathrm{c}}\mathbf{V}^* \tag{31}$$

where $\mathbf{G}_{\mathrm{c}} = \mathrm{diag}\{G_i^{\mathrm{c}}\}$ is the transfer-function matrix. Substituting (29) in (31) yields

$$\mathbf{V} = \mathbf{G}_{\mathrm{c}}\left((\mathbf{I}_N + \mathbf{H})\mathbf{V}_{\mathrm{ref}} - \mathbf{H}\bar{\mathbf{V}} - \left(c\mathbf{G}\mathbf{L}\mathbf{I}^{-1}_{\mathrm{rated}} + \mathbf{r}\right)\mathbf{I}\right). \tag{32}$$

The voltage observer dynamics are formulated in (21)–(23). By neglecting the disturbance in the observers, one can write $\bar{\mathbf{V}} = \mathbf{H}^{\mathrm{F}}_{\mathrm{obs}}\mathbf{V}$. The microgrid admittance matrix $\mathbf{Y}_{\mathrm{bus}}$ relates the supplied currents to the bus voltages as

$$\mathbf{I} = \mathbf{Y}_{\mathrm{bus}}\mathbf{V}. \tag{33}$$

The admittance matrix carries all the details of the distribution grid. For example, π-circuit model of any line can be considered by including the line series resistance, series inductance, and parallel capacitance in the admittance matrix $\mathbf{Y}_{\mathrm{bus}}$. Therefore, (32) can be written as

$$\begin{cases} \mathbf{V} &= \left(\mathbf{G}_{\mathrm{c}}^{-1} + \mathbf{H}\mathbf{H}^{\mathrm{F}}_{\mathrm{obs}} + \left(c\mathbf{G}\mathbf{L}\mathbf{I}^{-1}_{\mathrm{rated}} + \mathbf{r}\right)\mathbf{Y}_{\mathrm{bus}}\right)^{-1} \\ & \quad (\mathbf{I}_N + \mathbf{H})\mathbf{V}_{\mathrm{ref}} \\ \mathbf{I} &= \left((\mathbf{Y}_{\mathrm{bus}}\mathbf{G}_{\mathrm{c}})^{-1} + \mathbf{H}\mathbf{H}^{\mathrm{F}}_{\mathrm{obs}}\mathbf{Y}^{-1}_{\mathrm{bus}} + c\mathbf{G}\mathbf{L}\mathbf{I}^{-1}_{\mathrm{rated}} + \mathbf{r}\right)^{-1} \\ & \quad (\mathbf{I}_N + \mathbf{H})\mathbf{V}_{\mathrm{ref}}. \end{cases} \tag{34}$$

Equation (34) represents the global microgrid dynamics with the proposed controller in effect.

B. Controller Design Guidelines

For a given microgrid, the matrix of converters' closed-loop transfer functions $\mathbf{G}_{\rm c}$, the current rating matrix $\mathbf{I}_{\rm rated}$, and the admittance matrix $\mathbf{Y}_{\rm bus}$ are known. The communication graph needs to contain at least a spanning tree. Weights of the communication links a_{ij} and, thus, the Laplacian matrix $\mathbf{L}$, may, then, be chosen to provide the desired dynamic for the voltage observers by evaluating (7). It should be noted that the selection of the communication weights must satisfy a balanced Laplacian matrix. Equation (23) helps to design the coupling gain b, and the integrator gain matrix $\mathbf{K}$, to achieve a satisfactory noise cancellation dynamic. Given the Laplacian matrix $\mathbf{L}$, and the total observer transfer function $\mathbf{H}_{\rm obs}^{\rm F}$ (or the reduced-order function $\mathbf{H}_{\rm obs}$), one can use (34) to design the voltage and current controller matrices ($\mathbf{H}$ and $\mathbf{G}$, respectively), the virtual impedance matrix $\mathbf{r}$, and the coupling gain c to provide any desired asymptotically stable dynamic response, where all poles of (34) lie in the open left hand plane (OLHP). The current regulator surpasses the droop mechanism in providing the proportional load sharing and, thus, the virtual impedance matrix $\mathbf{r}$ can be freely designed. However, the designer may still use the traditional approach to tune the virtual impedances as

$$\mathbf{r} = m\mathbf{I}_{\rm rated}^{-1} \tag{35}$$

where m is a positive scalar design parameter.

C. Steady-State Analysis

Steady-state analysis is essential to ensure that the proposed controller satisfies both operational requirements; the global voltage regulation and the proportional load sharing. With no loss of generality, one can assume

$$\mathbf{V}_{\rm ref} = \frac{v_{\rm ref}}{s}\,\underline{\mathbf{1}} \tag{36}$$

where $v_{\rm ref}$ is the reference voltage for the entire microgrid. Voltage stabilization, throughout the microgrid, is also assumed. Accordingly, the voltage vector $\mathbf{V}$ is a type-1 vector, i.e., it has a single pole at the origin and all other poles lie in the OLHP. Thus, one may safely use the final value theorem to find the steady-state voltage vector $\mathbf{v}^{\rm ss}$

$$\begin{aligned}\mathbf{v}^{\rm ss} &= \lim_{t\to\infty}\mathbf{v}(t) = \lim_{s\to 0} s\mathbf{V}(s)\\ &= \lim_{s\to 0}\left(s\mathbf{G}_{\rm c}^{-1} + s\mathbf{H}\mathbf{H}_{\rm obs}^{\rm F} + s\left(c\mathbf{G}\mathbf{L}\mathbf{I}_{\rm rated}^{-1} + \mathbf{r}\right)\mathbf{Y}_{\rm bus}\right)^{-1}\\ &\quad\times sv_{\rm ref}(\mathbf{I}_N + \mathbf{H})\,\underline{\mathbf{1}}.\end{aligned} \tag{37}$$

The voltage and current controllers (H_is and G_is, respectively) are PI controllers and, thus, one can write $\mathbf{H} = \mathbf{H}_{\rm P} + \mathbf{H}_{\rm I}/s$, where $\mathbf{H}_{\rm P}$ and $\mathbf{H}_{\rm I}$ are diagonal matrices carrying proportional and integral gains of the voltage controllers. Similarly, $\mathbf{G} = \mathbf{G}_{\rm P} + \mathbf{G}_{\rm I}/s$, where $\mathbf{G}_{\rm P}$ and $\mathbf{G}_{\rm I}$ are diagonal matrices that contain proportional and integral gains of the current controllers. It is also known that the dc gain of the closed-loop converters are equal to one, i.e., $\mathbf{G}_{\rm c}(0) = \mathbf{I}_N = \mathbf{G}_{\rm c}^{-1}(0)$ [58]. In addition,

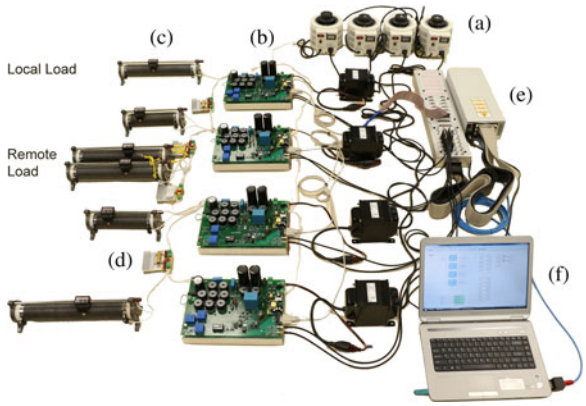

Fig. 5. DC microgrid prototype. (a) Input ac sources. (b) Buck converters driving each source. (c) Local and remote loads. (d) Transmission lines. (e) dSAPCE control board (DS1103). (f) Programming and monitoring PC.

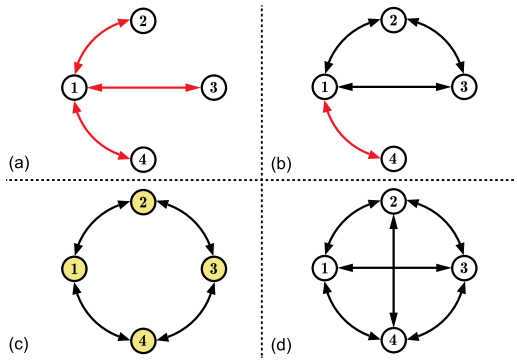

Fig. 6. Alternative connections forming a connected graph with: (a) No redundant link. (b) Suboptimal link redundancy. (c) Optimal link redundancy. (d) Full connection.

based on Theorem A.2 (see Appendix II), $\lim_{s\to 0}\mathbf{H}_{\rm obs}^{\rm F} = \mathbf{Q}$. Thus, (37) can be written as

$$\mathbf{v}^{\rm ss} = v_{\rm ref}\left(\mathbf{H}_{\rm I}\mathbf{Q} + c\mathbf{G}_{\rm I}\mathbf{L}\mathbf{I}_{\rm rated}^{-1}\mathbf{Y}_{\rm dc}\right)^{-1}\mathbf{H}_{\rm I}\,\underline{\mathbf{1}} \tag{38}$$

or, equivalently

$$\left(\mathbf{U}\mathbf{Q} + c\mathbf{L}\mathbf{I}_{\rm rated}^{-1}\mathbf{Y}_{\rm dc}\right)\mathbf{v}^{\rm ss} = v_{\rm ref}\mathbf{U}\,\underline{\mathbf{1}} \tag{39}$$

where $\mathbf{Y}_{\rm dc}{=}\mathbf{Y}_{\rm bus}(0)$ is the dc admittance matrix and $\mathbf{U} = \mathbf{G}_{\rm I}^{-1}\mathbf{H}_{\rm I} = {\rm diag}\{u_i\}$ is a diagonal matrix with $u_i = \mathbf{H}_{\rm I}(i,i)/\mathbf{G}_{\rm I}(i,i)$. All the integrator gains for the current controllers are assumed to be positive and, thus, $\mathbf{G}_{\rm I}^{-1}$ exists. Since the Laplacian matrix is designed to be balanced (see Section V-B), one can write $\mathbf{Q}\mathbf{L} = \mathbf{0}$. Therefore, by multiplying both sides of (39) by the averaging matrix $\mathbf{Q}$

$$\mathbf{Q}\left(\mathbf{U}\left(\mathbf{Q}\mathbf{v}^{\rm ss}\right)\right) = v_{\rm ref}\mathbf{Q}\left(\mathbf{U}\,\underline{\mathbf{1}}\right). \tag{40}$$

Based on the definition of the averaging matrix $\mathbf{Q}$, $\mathbf{Q}\mathbf{x} = \langle\mathbf{x}\rangle\,\underline{\mathbf{1}}$, for any vector $\mathbf{x}\in\mathbb{R}^{N\times 1}$. Accordingly, (40) is equivalent to

$$\langle\mathbf{v}^{\rm ss}\rangle\,\langle\mathbf{U}\,\underline{\mathbf{1}}\,\rangle\,\underline{\mathbf{1}} = v_{\rm ref}\,\langle\mathbf{U}\,\underline{\mathbf{1}}\,\rangle\,\underline{\mathbf{1}} \tag{41}$$

or, equivalently, $\langle\mathbf{v}^{\rm ss}\rangle = v_{\rm ref}$. This analysis shows that the proposed controller provides global voltage regulation, i.e., it

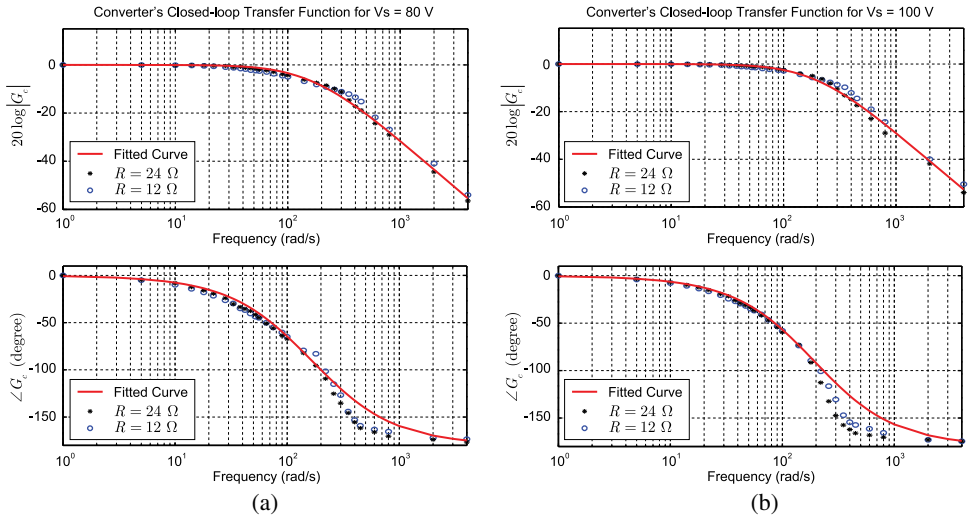

Fig. 7. Measured frequency response of the buck converters for various operating conditions. (a) $V_{\rm s} = 80$ V, (b) $V_{\rm s} = 100$ V.

successfully regulates the average voltage at the desired value. On the other hand, (39) can be written as

$$\mathbf{U}\left(\mathbf{Q}\mathbf{v}^{\rm ss}\right) + c\mathbf{L}\mathbf{I}_{\rm rated}^{-1}\mathbf{i}^{\rm ss} = v_{\rm ref}\mathbf{U}\,\underline{\mathbf{1}} \tag{42}$$

or, equivalently,

$$\mathbf{L}\left(\mathbf{I}_{\rm rated}^{-1}\mathbf{i}^{\rm ss}\right) = c^{-1}\left(v_{\rm ref} - \langle\mathbf{v}^{\rm ss}\rangle\right)\mathbf{U}\,\underline{\mathbf{1}} = \mathbf{0}. \tag{43}$$

The Lemma A.1 (see Appendix I) ensures that the Laplacian matrix $\mathbf{L}$ has a simple eigenvalue at the origin, i.e., $\lambda_1 = 0$. Thus, based on (43), $\mathbf{I}_{\rm rated}^{-1}\mathbf{i}^{\rm ss}$ is the right eigenvector of $\mathbf{L}$ associated with $\lambda_1 = 0$. It is mentioned in the Proof of Lemma A.2 (see Appendix I) that $w_r =$ is the right eigenvector of the Laplacian matrix $\mathbf{L}$ associated with $\lambda_1 = 0$. Thus

$$\mathbf{I}_{\rm rated}^{-1}\mathbf{i}^{\rm ss} = n\underline{\mathbf{1}} \tag{44}$$

where n is a positive scalar. Equation (44) concludes the proportional load sharing. Equations (41) and (44) show that the proposed controller successfully carries out both global voltage regulation and proportional load sharing.

VI. Case Study

A low-voltage dc microgrid, with a structure shown in Fig. 2, is prototyped to study the proposed control methodology. Fig. 5 shows the experimental setup. Four adjustable isolated ac sources are used as the energy sources. Each source is driven by a buck converter augmented with an input rectifier. The converters have similar topologies but different ratings, i.e., the rated currents of the first and the fourth converters are twice those for the other two converters. A π-circuit model is used for each transmission line. There are four local and one remote loads, as seen in Fig. 2.

Alternative graphical connections are shown in Fig. 6. Communication links are assumed bidirectional to feature a balanced

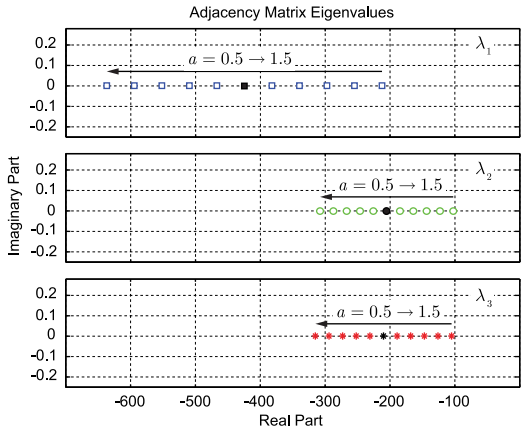

Fig. 8. Movement of the eigenvalues of the adjacency matrix as the scaling coefficient changes.

Laplacian matrix and help with the sparsity of the resulting communication graph. Although all alternative graphs include spanning trees, some are susceptible to lose connectivity in the case of a single link failure. For example, if any of the links highlighted in red in Fig. 6(a) or (b) is lost, the corresponding graph losses its connectivity, which hinders the functionality of the control mechanism. However, for the set of four agents, the circular communication flow in Fig. 6(c) is the sparsest network where the failure of a single link does not compromise the graphical connectivity. Fig. 6(d) is a fully connected graph, but it lacks sparsity. Therefore, the graphical structure in Fig. 6(c) is chosen for data exchange in the cyber layer.

A dSPACE control board (DS1103) implements the control routines. Electrical parameters of the microgrid are provided in the Appendix III. Although different voltage levels are possible [60], [61], a 48 V system is considered here. The typical acceptable voltage deviation is about 5% of the rated voltage [36] and, thus, the voltage limiters are set accordingly with $\varepsilon = 2.5$ V.

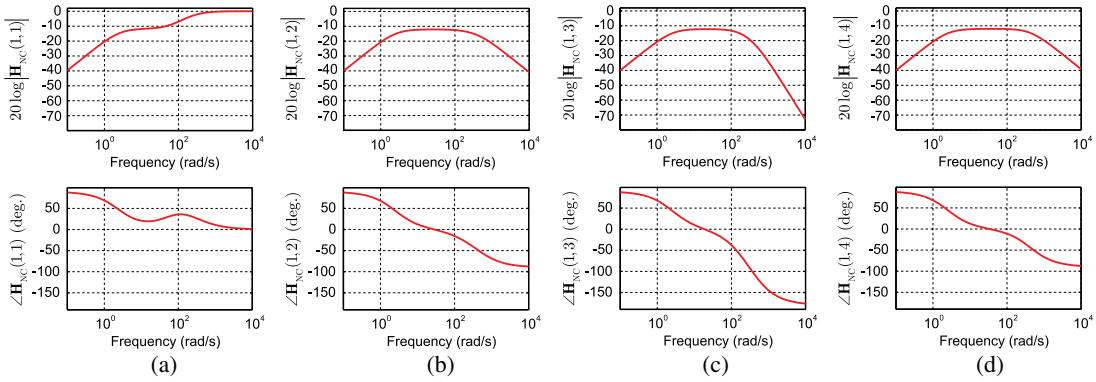

Fig. 9. Frequency response of the noise-cancellation module at the first node. (a) $\mathbf{H}_{\mathrm{NC}}(1,1)$, (b) $\mathbf{H}_{\mathrm{NC}}(1,2)$, (c) $\mathbf{H}_{\mathrm{NC}}(1,3)$, (d) $\mathbf{H}_{\mathrm{NC}}(1,4)$.

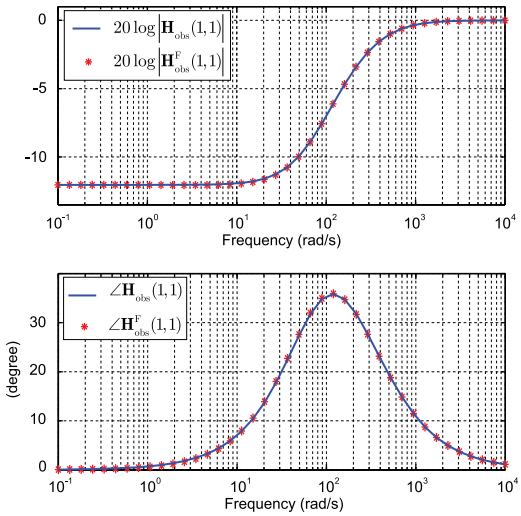

Fig. 10. Comparison of the reduced-order observers' dynamic, $\mathbf{H}_{\mathrm{obs}}(1,1)$, and the total observers' dynamic, $\mathbf{H}^{\mathrm{F}}_{\mathrm{obs}}(1,1)$.

A. Design Procedure

Prior knowledge of converters' frequency response is essential to the design procedure in Section V-B. Dynamic modeling of power electronics converters for microgrid applications is discussed in detail in the literature [62]. Analytical approaches do not consider practical limitations such as constraints on the duty cycles of switching converters. Alternatively, the transfer functions of the underlying converters are extracted experimentally using perturbation injection and frequency sweep techniques. For a wide range of loading conditions and input voltages, the reference point of each converter is augmented with a sinusoidal signal with an adjustable frequency. For any given frequency point, the sinusoidal content of the converter's output voltage is then compared with the injected sinusoidal signal to extract the converter's frequency response for that given frequency. This procedure is repeated for the frequency range of interest. Output impedances are chosen in the study to cover light load ($R = 24\ \Omega$) to full load ($R = 12\ \Omega$) conditions. Measured transfer functions are shown in Fig. 7. Accordingly, the converter's transfer function can be formulated as a second-order function

$$G_i^{\mathrm{c}} = \frac{|p_1|\,|p_2|}{(s-p_1)(s-p_2)} \tag{45}$$

where p_1 and p_2 ($|p_2| > |p_1|$) can be found by curve-fitting techniques. Fitted frequency response is highlighted in red in Fig. 7, where a good agreement is reported between the empirical and fitted data. The transfer function in (45) is further used in the design procedure.

Following the guideline in Section V-B, knowledge of the microgrid admittance matrix is also required. The underlying microgrid is a five-bus system (see Fig. 2) and has a 5×5 admittance matrix. However, the admittance matrix $\mathbf{Y}_{\mathrm{bus}}$ in (33) only represents the interaction between the voltages and currents of the generating buses and, thus, is a 4×4 matrix. This matrix can be found by reducing the original 5×5 admittance matrix through the Kron's reduction technique.

Design of the communication weights a_{ij}s, which are stored in the adjacency matrix $\mathbf{A_G}$ (or, equivalently, the Laplacian matrix $\mathbf{L}$) is tightly linked to the voltage observers' dynamic in (7). The weights can be designed to adjust the convergence speed of the estimated voltages. Proper functioning of the voltage regulator in Fig. 2 requires a fast estimation of the global average voltage, particularly, faster than the converters' dynamic. Here, it is desired that the eigenvalues of the adjacency matrix (or, equivalently, poles of $\mathbf{H}_{\mathrm{obs}}$) provide a dynamic estimation response at least twice as fast as that of the converters'. A scaling factor a is defined to scale the adjacency matrix as

$$\mathbf{A_G} = a \times \begin{bmatrix} 0 & 90 & 0 & 110 \\ 90 & 0 & 100 & 0 \\ 0 & 100 & 0 & 120 \\ 110 & 0 & 120 & 0 \end{bmatrix}. \tag{46}$$

Fig. 8 shows how the eigenvalues of the adjacency matrix vary as the scaling coefficient a changes from 0.5 to 1.5. The dominant pole of the converters' transfer function is $p_1 = -106$. Eigenvalues of $\mathbf{A_G}$, λ_ks are highlighted in Fig. 8 in black for $a = 1$, where $\forall k \leq 3$, $|\mathrm{real}(\lambda_k)| > 2 \times |\mathrm{real}(p_1)|$. Therefore, $a = 1$ provides an appropriate scaling coefficient for the adjacency matrix in (46). It should be noted that the nonzero matrix entries

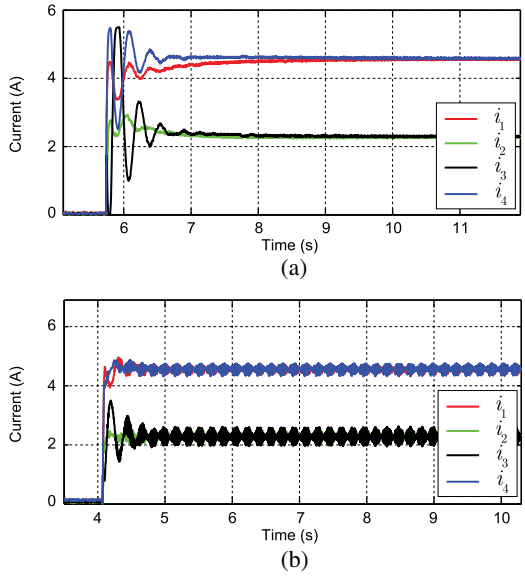

Fig. 11. Current regulating performance for small and large coupling gains; measured output currents for: (a) $c = 0.005$ stable and very slow, (b) $c = 0.15$ fast and resonating.

in (46) are arbitrarily chosen and other selections are viable; however, they might result in a different optimal scaling factor.

The performance of the noise-cancellation module is evaluated numerically using (23). The coupling gain b and the NC integrator gain matrix $\mathbf{K}$ are chosen (see Appendix III) to provide higher than 65% attenuation for disturbances with $f_{\text{noise}} < 5$ Hz. The noise-cancellation transfer function $\mathbf{H}_{\text{NC}}$ is plotted in Fig. 9 for the first node. As seen, all terms of $\mathbf{H}_{\text{NC}}$ are stable functions and exhibit satisfactory attenuations as demonstrated by the low gain at low frequencies. This implies successful noise rejection for dc and low-frequency disturbances. Similar performance is observed for the NC modules at other nodes.

Comparison between (7) and (22) shows that NC modules can affect the observers' transfer function. Proper selection of the coupling gain b and the matrix $\mathbf{K}$ can significantly suppress this impact. Fig. 10 compares the first entry $(1, 1)$ of the total observers' transfer function $\mathbf{H}_{\text{obs}}^{\text{F}}$ with the reduced-order function $\mathbf{H}_{\text{obs}}$, where it can be seen that the NC module has a negligible impact on observers' frequency response. A similar match is observed between other entries of $\mathbf{H}_{\text{obs}}^{\text{F}}$ and corresponding entries of $\mathbf{H}_{\text{obs}}$. Accordingly, one can safely assume $\mathbf{H}_{\text{obs}}^{\text{F}} = \mathbf{H}_{\text{obs}}$.

The current regulator module carries out the load sharing regardless of the selection of the droop coefficients. However, the choice of the coefficients based on (35) improves the load sharing dynamics. Accordingly, $m = 3$ is chosen here, which results in the virtual impedance matrix $\mathbf{r}$, provided in Appendix III.

The coupling gain between the current and the voltage regulator c determines load sharing dynamics. Fig. 11 compares the measured dynamic response of the microgrid for two different values of c. Small coupling gain c can slow down the system while a large coupling gain can lead to resonance or even make the system unstable. A medium value is adopted here, i.e., $c = 0.075$. Satisfactory system performance is verified empirically. Although (34) provides analytical evaluation of system dynamic, it does not consider limitations such as constraint on the duty cycle of the switching converters and, thus, empirical performance evaluation is preferred instead. Design parameters are summarized in the Appendix III. As seen, dissimilar control parameters are selected for different converters to verify controller performance in the case of heterogeneous agents (sources).

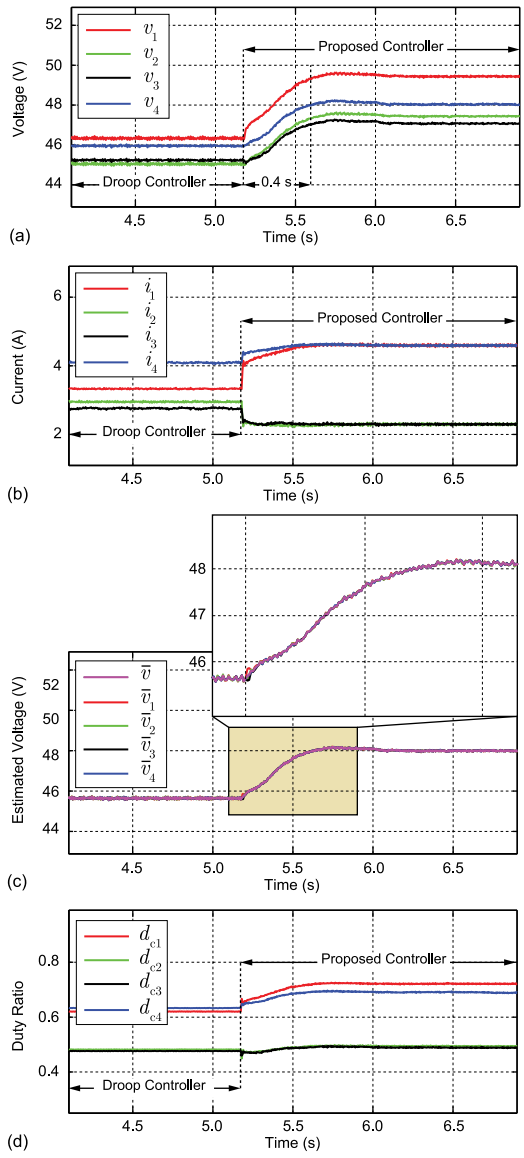

Fig. 12. Comparative studies of the conventional droop control and the proposed controller. (a) Terminal voltages. (b) Supplied currents. (c) Estimations of the average voltage. (d) Converters' duty ratios.

B. Droop Controller Versus Proposed Controller

Fig. 12 comparatively studies the performance of the proposed methodology. The microgrid is initially controlled using the conventional droop controller. It leads to voltages less than the desired value, i.e., $v_{\text{ref}} = 48$ V. In addition, although the droop gains are designed reciprocal to the

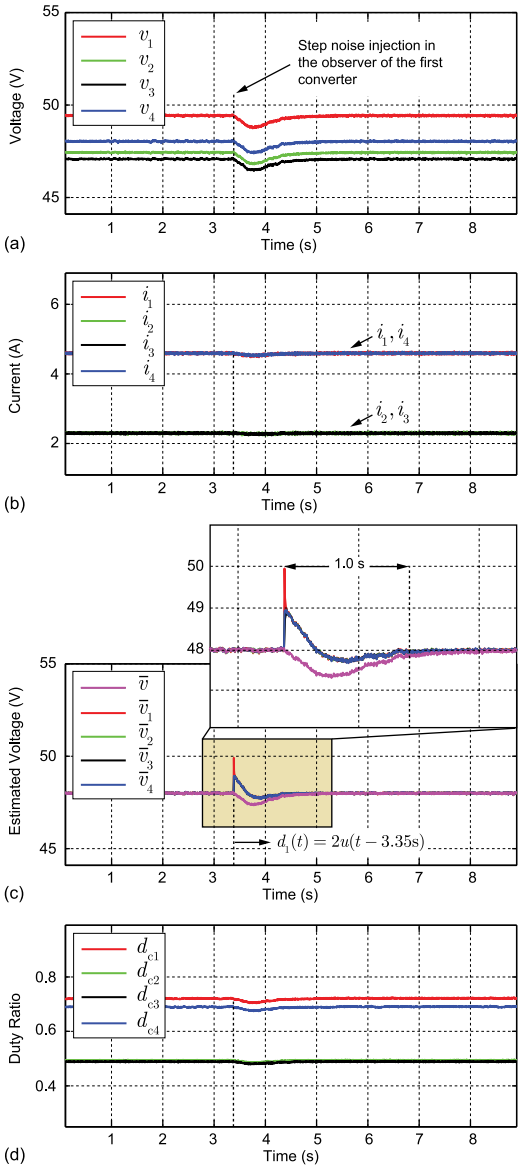

Fig. 13. Performance of the noise cancellation mechanism. (a) Terminal voltages. (b) Supplied currents. (c) Estimations of the average voltage. (d) Converters' duty ratios.

converters' rated currents, the transmission line effects have clearly incapacitated the droop mechanism resulting in a poor load sharing. The proposed controller is engaged at $t = 5.18$ s. Consequently, the voltages are all boosted across the microgrid and the average voltage is finely regulated at the set point, i.e., $v_{\text{ref}} = 48$ V. Fig. 12(b) shows that the proportional load sharing is also carried out, where the first and the fourth converters carry twice the current as the other two converters. Performance of the voltage observers is studied in Fig. 12(c), where a good agreement is seen between the true average voltage $\bar{v}$ and the individual estimated voltages $\bar{v}_i$s.

The efficacy of the noise cancellation module is studied in Fig. 13, where a step disturbance, i.e., $d_1(t) = 2u(t - 3.35\text{ s})$, is intentionally applied to the estimation at node one. It can be seen in Fig. 13(c) that the disturbance causes sudden increase in all

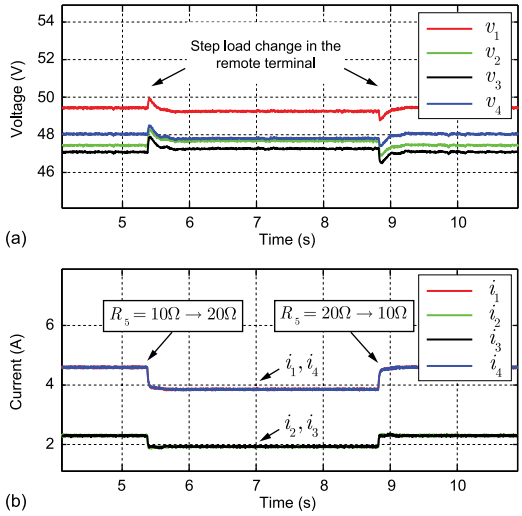

Fig. 14. Performance of the cooperative distributed controller in a case of load change. (a) Terminal voltages. (b) Supplied currents.

estimations. Accordingly, the controller has slightly decreased the duty ratios. Simultaneously, the NC module has identified the noise and adjusted the cancellation term $\hat{d}_1$ to neutralize the noise impact. Consequently, all estimations are recovered in less than 1 s and continue tracking the true average voltage $\bar{v}$. Fig. 13(a) and (b) shows that the NC module has effectively eliminated the noise impact on the voltage regulation and the load sharing.

C. Load Change Performance Assessment

The controller performance in case of load change is studied in Fig. 14, where the remote load at bus five R_5 is changed in step between 10 Ω and 20 Ω. Tight voltage regulation and load sharing can be observed in this figure. Excellent transient load sharing is also noticeable in Fig. 14(b).

D. Plug-and-Play Capability

Fig. 15 studies plug-and-play capability of the proposed method and its performance in case of a converter failure. As seen, when the second converter fails, the controller readjusts the voltages to satisfy the global voltage regulation. It also readjusts the load sharing among the remaining converters. It should be noted that a converter failure also implies loss of all communication links connected to that particular converter. Accordingly, when the second converter fails, it automatically renders the links 1-2 (between nodes 1 and 2) and 2-3 inoperable. However, the remaining links still form a connected graph with balanced Laplacian matrix [see Fig. 6(c)]. Then, the second converter is plugged back in at $t = 12.1$ s. As seen, the controller has properly updated the load sharing, and global voltage regulation, after the second converter is plugged in.

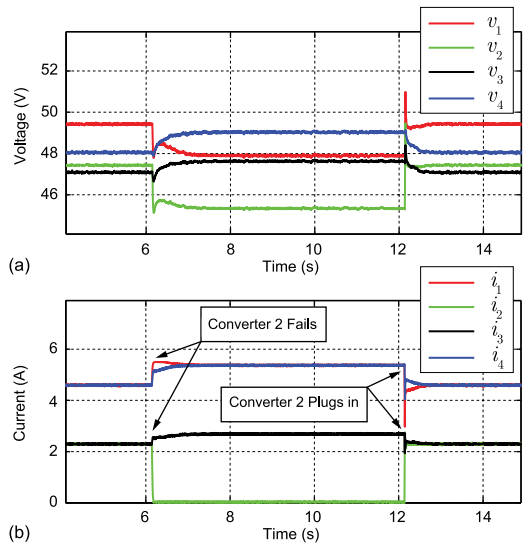

Fig. 15. Converter failure and plug-and-play studies. (a) Terminal voltages. (b) Supplied currents.

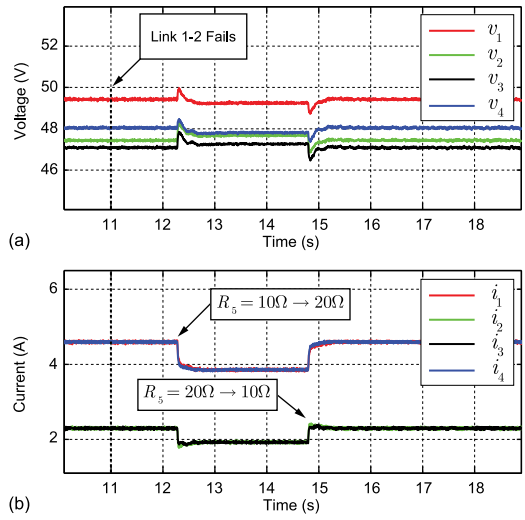

Fig. 16. Link-failure resiliency. (a) Terminal voltages. (b) Supplied currents.

E. Link-Failure Resiliency

Resiliency to a single link failure is studied next in Fig. 16. The original communication graph is designed to carry a minimum redundancy, so no single link failure can cause loss of graphical connectivity. Thus, the control system shall remain operational. As seen in Fig. 16, the links 1-2 has failed at $t = 11$ s, but it does not have any impact on voltage regulation or load sharing.

Response of the controller to the step load change in the remote load is also studied with the failed link, where a satisfactory performance can be seen. It should be noted that the reconfiguration caused by the link failure affects the Laplacian matrix and, thus, the whole system dynamic. Comparing Figs. 14(b) and 16(b), one can see that the link failure slightly slows the controller transient response.

VII. Conclusion

A distributed secondary/primary controller is proposed for dc microgrids. The controller on each converter has two modules; the voltage regulator and the current regulator. The voltage regulator uses a noise-resilient voltage observer to estimate the global average voltage. This estimation is then further used to adjust the local voltage set point to provide global voltage regulation. The current regulator compares local per-unit current with its neighbors' per-unit currents and, accordingly, adjusts the voltage set point to carry out proportional load sharing. This control paradigm uses a sparse communication network for data exchange. Studies show that the proposed cooperative control provides precise global voltage regulation and proportional load sharing. Noise resiliency of the proposed voltage observer and link-failure resiliency of the overall control structure are also verified through experiments.

Appendix I

Dynamic Consensus

Following lemmas need to be studied before studying the dynamic consensus:

Lemma A.1 [54]: Assume that the digraph $\mathbf{G}$ has a spanning tree. Then, the Laplacian matrix $\mathbf{L}$ has a simple eigenvalue at the origin, i.e., $\lambda_1 = 0$ and other eigenvalues lie in the open right hand plane (ORHP). In addition

$$\lim_{t\to\infty} e^{-\mathbf{L}t} = w_r w_l^{\mathrm{T}} \tag{A.1}$$

where $w_r \in \mathbb{R}^{N\times 1}$ and $w_l^{\mathrm{T}} \in^{N\times 1}$ are the right and left eigenvectors of $\mathbf{L}$ associated with $\lambda_1 = 0$, respectively. It should be noted that w_l^{T} should be normalized with respect to w_r, i.e., $w_l^{\mathrm{T}} w_r = 1$.

Lemma A.2: Assume that the digraph $\mathbf{G}$ has a spanning tree and the Laplacian matrix $\mathbf{L}$ is balanced. Then

$$\lim_{s\to 0} s(s\mathbf{I}_N + \mathbf{L})^{-1} = \mathbf{Q}. \tag{A.2}$$

$$\lim_{s\to 0} \mathbf{L}(s\mathbf{I}_N + \mathbf{L})^{-1} = \lim_{s\to 0}(s\mathbf{I}_N + \mathbf{L})^{-1}\mathbf{L} = \mathbf{I}_N - \mathbf{Q} \tag{A.3}$$

where $\mathbf{Q}$ is the averaging matrix defined in Section IV-A.

Proof of Lemma A.2: Assume a linear system of $\dot{\mathbf{x}} = -\mathbf{L}\mathbf{x}$ with $\mathbf{x}(0) \neq \mathbf{0}$ and $\mathbf{x} \in \mathbb{R}^{N\times 1}$. One can write

$$\mathbf{x}(t) = e^{-\mathbf{L}t}\mathbf{x}(0) \tag{A.4}$$

or, equivalently, in the frequency domain

$$\mathbf{X} = (s\mathbf{I}_N + \mathbf{L})^{-1}\mathbf{x}(0). \tag{A.5}$$

Lemma A.1 ensures that $\mathbf{X}$ is a type-1 vector, i.e., it has a single pole at the origin and all other poles lie in the OLHP. Thus, using the final value theorem

$$\lim_{t\to\infty} \mathbf{x}(t) = \lim_{s\to 0} s\mathbf{X} = \left(\lim_{s\to 0} s(s\mathbf{I}_N + \mathbf{L})^{-1}\right)\mathbf{x}(0). \tag{A.6}$$

On the other hand, by using Lemma A.1, (A.4) yields to

$$\lim_{t\to\infty} \mathbf{x}(t) = \left(\lim_{t\to\infty} e^{-\mathbf{L}t}\right)\mathbf{x}(0) = w_r w_l^{\mathrm{T}}\mathbf{x}(0). \tag{A.7}$$

For any Laplacian matrix $\mathbf{L}$, all row sums are equal to zero. Thus, $w_r = \underline{1}$. In addition, for any balanced $\mathbf{L}$, all column sums are also equal to zero. Thus, $w_l = (1/N)\underline{1}$. Accordingly, (A.7) implies that

$$\lim_{t\to\infty} \mathbf{x}(t) = \mathbf{Q}\mathbf{x}(0). \tag{A.8}$$

Comparing (A.6)–(A.8)

$$\left(\lim_{s\to 0} s(s\mathbf{I}_N + \mathbf{L})^{-1}\right)\mathbf{x}(0) = \mathbf{Q}\mathbf{x}(0). \tag{A.9}$$

Since (A.9) holds for all $\mathbf{x}(0) \neq \mathbf{0}$, one may conclude (A.2). In addition

$$\begin{aligned}\mathbf{I}_N &= \lim_{s\to 0}(s\mathbf{I}_N + \mathbf{L})(s\mathbf{I}_N + \mathbf{L})^{-1} \\ &= \lim_{s\to 0} s(s\mathbf{I}_N + \mathbf{L})^{-1} + \lim_{s\to 0}\mathbf{L}(s\mathbf{I}_N + \mathbf{L})^{-1}. \end{aligned}\tag{A.10}$$

Comparing (A.2) with (A.10) concludes (A.3). □

Theorem A.1: Assume that the communication graph $\mathbf{G}$ used in a cooperative control system, has a spanning tree and the associated Laplacian matrix $\mathbf{L}$ is balanced. Then, using the observer in (7), all the estimated averages in $\bar{\mathbf{v}}$ converge to the true global average voltage.

Proof of Theorem A.1: Equation (34) shows the global dynamic of the microgrid, when the proposed controller is effective. It is assumed that the system parameters are, accordingly, designed to stabilize the microgrid. Thus, the resulting voltage vector $\mathbf{V}$ is a type-1 vector. Based on Lemma A.1, all poles of the term $s(s\mathbf{I}_N + \mathbf{L})^{-1}$ lie in the OLHP. It should be noted that if λ_i is an eigenvalue of $\mathbf{L}$ then, $s = -\lambda_i$ is a pole of $s(s\mathbf{I}_N + \mathbf{L})^{-1}$. The term s in $s(s\mathbf{I}_N + \mathbf{L})^{-1}$ cancels the pole of $(s\mathbf{I}_N + \mathbf{L})^{-1}$ at the origin. Thus, (7) implies that $\bar{\mathbf{V}}$ is also a type-1 vector. Since both $\mathbf{V}$ and $\bar{\mathbf{V}}$ are type 1, one may use the final value theorem

$$\lim_{t\to\infty}\bar{\mathbf{v}}(t) = \lim_{s\to 0} s\bar{\mathbf{V}} = \lim_{s\to 0} s(s\mathbf{I}_N + \mathbf{L})^{-1}(s\mathbf{V}). \tag{A.11}$$

Using Lemma A.2

$$\begin{aligned}\lim_{t\to\infty}\bar{\mathbf{v}}(t) &= \lim_{s\to 0} s(s\mathbf{I}_N + \mathbf{L})^{-1} \times \lim_{s\to 0}(s\mathbf{V}) \\ &= \mathbf{Q} \times \lim_{t\to\infty}\mathbf{v} = \mathbf{Q}\mathbf{v}^{\mathrm{ss}} = \langle \mathbf{v}^{\mathrm{ss}}\rangle\,\underline{1}. \end{aligned}\tag{A.12}$$

Equation (A.12) implies that all estimations converge to the true global average voltage. In other words

$$\forall i : 0 \le i \le N, \quad \lim_{t\to\infty}\bar{v}_i(t) = \tfrac{1}{N}\sum_{i=1}^{N} v_i(t)\,. \tag{A.13}$$

■

APPENDIX II
ANALYSIS OF THE NOISE CANCELLATION MODULE

Following lemmas need to be studied before analyzing the noise cancellation module:

Lemma A.3: For a given matrix $\mathbf{A} \in \mathbb{R}^{N\times N}$, if $\mathbf{I}_N + \mathbf{A}^{-1}$ is invertible then

$$(\mathbf{I}_N + \mathbf{A})^{-1} = \mathbf{I}_N - \mathbf{A}(\mathbf{I}_N + \mathbf{A})^{-1} = \mathbf{I}_N - (\mathbf{I}_N + \mathbf{A})^{-1}\mathbf{A}. \tag{A.14}$$

Proof of Lemma A.3: For a given matrix $\mathbf{A} \in \mathbb{R}^{N\times N}$

$$\begin{aligned}(\mathbf{I}_N + \mathbf{A})^{-1} &= (\mathbf{I}_N + \mathbf{A})^{-1}(\mathbf{I}_N + \mathbf{A}) - (\mathbf{I}_N + \mathbf{A})^{-1}\mathbf{A} \\ &= \mathbf{I}_N - (\mathbf{I}_N + \mathbf{A})^{-1}\mathbf{A}.\end{aligned}$$

□

Lemma A.4: For a given invertible matrix $\mathbf{A} \in \mathbb{R}^{N\times N}$ if $\mathbf{I}_N + \mathbf{A}$ is invertible then

$$(\mathbf{I}_N + \mathbf{A}^{-1})^{-1} = \mathbf{A}(\mathbf{I}_N + \mathbf{A})^{-1} = (\mathbf{I}_N + \mathbf{A})^{-1}\mathbf{A}. \tag{A.15}$$

Proof of Lemma A.4: For a given invertible matrix $\mathbf{A}$

$$\begin{aligned}(\mathbf{I}_N + \mathbf{A}^{-1})^{-1} &= (\mathbf{A}\mathbf{A}^{-1} + \mathbf{A}^{-1})^{-1} = \left((\mathbf{I}_N + \mathbf{A})\mathbf{A}^{-1}\right)^{-1} \\ &= \mathbf{A}(\mathbf{I}_N + \mathbf{A})^{-1}.\end{aligned}$$

Lemma A.5: If $\mathbf{L}$ is a balanced Laplacian matrix, $b > 0$ and $\mathbf{K} = \mathrm{diag}\{k_i\}$ has positive diagonal elements then, $\mathbf{L}' = b\mathbf{L}\mathbf{K}^{-1}\mathbf{L}$ is a balanced Laplacian matrix.

Proof of Lemma A.5: The matrix $\mathbf{L}$ is said to be a Laplacian matrix if a communication graph exists with the associated Laplacian matrix $\mathbf{L}$. Equivalently, a matrix is a Laplacian matrix if and only if $\mathbf{L}\underline{1} = \mathbf{0}$. A Laplacian matrix is balanced if it has all column-sums of zero, i.e., $\underline{1}^{\mathrm{T}}\mathbf{L} = \mathbf{0}$. Let $\mathbf{L}$ be a balanced Laplacian matrix and $\mathbf{L}' = b\mathbf{L}\mathbf{K}^{-1}\mathbf{L}$ then

$$\mathbf{L}'\underline{1} = b\mathbf{L}\mathbf{K}^{-1}\left(\mathbf{L}\underline{1}\right) = \mathbf{0} \tag{A.16}$$

which implies that $\mathbf{L}'$ is a Laplacian matrix. On the other hand

$$\underline{1}^{\mathrm{T}}\mathbf{L}' = b\left(\underline{1}^{\mathrm{T}}\mathbf{L}\right)\mathbf{K}^{-1}\mathbf{L} = \mathbf{0} \tag{A.17}$$

which shows that $\mathbf{L}'$ is also balanced. □

Lemma A.6: If $\mathbf{L}$ is a balanced Laplacian matrix, $b > 0$, and $\mathbf{K} = \mathrm{diag}\{k_i\}$ has positive diagonal elements then

$$\lim_{s\to 0} s\left(s\mathbf{I}_N + (s\mathbf{I}_N + b\mathbf{L})\mathbf{K}^{-1}(s\mathbf{I}_N + \mathbf{L})\right)^{-1} = \mathbf{Q} \tag{A.18}$$

$$\lim_{s\to 0}\left(\mathbf{I}_N + s(s\mathbf{I}_N + \mathbf{L})^{-1}\mathbf{K}(s\mathbf{I}_N + b\mathbf{L})^{-1}\right)^{-1} = \mathbf{I}_N - \mathbf{Q}. \tag{A.19}$$

Proof of Lemma A.6: Let $\mathbf{L}$ be a balanced Laplacian matrix, $b > 0$, and $\mathbf{K} = \mathrm{diag}\{k_i\}$ has positive diagonal elements. Then

$$\lim_{s\to 0}\left((s\mathbf{I}_N + b\mathbf{L})\mathbf{K}^{-1}(s\mathbf{I}_N + \mathbf{L})\right) = b\mathbf{L}\mathbf{K}^{-1}\mathbf{L}. \tag{A.20}$$

Let us define $\mathbf{L}' = b\mathbf{L}\mathbf{K}^{-1}\mathbf{L}$. Then, using (A.20)

$$\begin{aligned}&\lim_{s\to 0} s\left(s\mathbf{I}_N + (s\mathbf{I}_N + b\mathbf{L})\mathbf{K}^{-1}(s\mathbf{I}_N + \mathbf{L})\right)^{-1} \\ &= \lim_{s\to 0} s\left(s\mathbf{I}_N + \mathbf{L}'\right)^{-1}.\end{aligned}\tag{A.21}$$

Lemma A.5 ensures that $\mathbf{L}'$ is a balanced Laplacian matrix. Therefore, by applying Lemma A.2 (A.2), one can write $\lim_{s\to 0} s(s\mathbf{I}_N + \mathbf{L}')^{-1} = \mathbf{Q}.$, which, together with (A.21), proves (A.18).

To study the second part of the Lemma, (A.19), one may note that for $s \neq 0$, $s\mathbf{I}_N + b\mathbf{L}$ is invertible [63]. $\mathbf{K}$ is also invertible and $\mathbf{K}^{-1} = \mathrm{diag}\{k_i^{-1}\}$. Let us define

$$\Gamma \triangleq \left(\mathbf{I}_N + s(s\mathbf{I}_N + \mathbf{L})^{-1}\mathbf{K}(s\mathbf{I}_N + b\mathbf{L})^{-1}\right)^{-1}. \tag{A.22}$$

Using Lemma A.3

$$\Gamma = \mathbf{I}_N - s(s\mathbf{I}_N + \mathbf{L})^{-1}\mathbf{K}(s\mathbf{I}_N + b\mathbf{L})^{-1} \times \left(\mathbf{I}_N + s(s\mathbf{I}_N + \mathbf{L})^{-1}\mathbf{K}(s\mathbf{I}_N + b\mathbf{L})^{-1}\right)^{-1}. \quad \text{(A.23)}$$

Lemma A.4 offers to further expand (A.23)

$$\begin{aligned}\Gamma &= \mathbf{I}_N - s(s\mathbf{I}_N + \mathbf{L})^{-1}\mathbf{K}(s\mathbf{I}_N + b\mathbf{L})^{-1}\frac{1}{s}(s\mathbf{I}_N + b\mathbf{L})\mathbf{K}^{-1} \\ &\quad \times (s\mathbf{I}_N + \mathbf{L})\left(\mathbf{I}_N + \frac{1}{s}(s\mathbf{I}_N + b\mathbf{L})\mathbf{K}^{-1}(s\mathbf{I}_N + \mathbf{L})\right)^{-1} \\ &= \mathbf{I}_N - s\left(s\mathbf{I}_N + (s\mathbf{I}_N + b\mathbf{L})\mathbf{K}^{-1}(s\mathbf{I}_N + \mathbf{L})\right)^{-1}.\end{aligned} \quad \text{(A.24)}$$

By applying Lemma A.6, (A.18)–(A.24) one can conclude $\lim_{s\to 0}\Gamma = \mathbf{I}_N - \mathbf{Q}$. □

Theorem A.2: Assume that the communication graph $\mathbf{G}$, used in a distributed control system, has a spanning tree, and the associated Laplacian matrix $\mathbf{L}$ is balanced. Then, using the total observer in (21)–(23), all the estimated averages in $\bar{\mathbf{v}}$ converge to the true global average voltage average.

Proof of Theorem A.2: For any $s \neq 0$, $(s\mathbf{I}_N + b\mathbf{L})$ is invertible [63]. The integrator gain matrix $\mathbf{K}$ is also invertible and $\mathbf{K}^{-1} = \mathrm{diag}\{k_i^{-1}\}$. Thus, one can safely reformulate the total observer transfer function as

$$\begin{aligned}\mathbf{H}_{\mathrm{obs}}^{\mathrm{F}} &= \left((s\mathbf{I}_N + \mathbf{L}) + s\mathbf{K}\,(s\mathbf{I}_N + b\mathbf{L})^{-1}\right)^{-1} \\ &\quad \times \left((s\mathbf{I}_N + \mathbf{L}) + s\mathbf{K}\,(s\mathbf{I}_N + b\mathbf{L})^{-1} - \mathbf{L}\right) \\ &= \mathbf{I}_N - \left((s\mathbf{I}_N + \mathbf{L}) + s\mathbf{K}\,(s\mathbf{I}_N + b\mathbf{L})^{-1}\right)^{-1}\mathbf{L} \\ &= \mathbf{I}_N - \big((s\mathbf{I}_N + \mathbf{L})\left(\mathbf{I}_N + s\,(s\mathbf{I}_N + \mathbf{L})^{-1}\right. \\ &\quad \left.\times\,\mathbf{K}\,(s\mathbf{I}_N + b\mathbf{L})^{-1}\right)\big)^{-1}\mathbf{L} \\ &= \mathbf{I}_N - \left(\mathbf{I}_N + s\,(s\mathbf{I}_N + \mathbf{L})^{-1}\,\mathbf{K}\,(s\mathbf{I}_N + b\mathbf{L})^{-1}\right)^{-1} \\ &\quad \times\,(s\mathbf{I}_N + \mathbf{L})^{-1}\,\mathbf{L}.\end{aligned} \quad \text{(A.25)}$$

Using Lemma A.2 (A.3) and Lemma A.6 (A.19), the total observer dc gain can be found

$$\lim_{s\to 0}\mathbf{H}_{\mathrm{obs}}^{\mathrm{F}} = \mathbf{I}_N - (\mathbf{I}_N - \mathbf{Q})^2 = 2\mathbf{Q} - \mathbf{Q}^2 = \mathbf{Q}. \quad \text{(A.26)}$$

Therefore, for type 1 (dc and exponentially damping) disturbances, (21) yields to

$$\begin{aligned}\lim_{t\to\infty}\bar{\mathbf{v}}(t) &= \lim_{s\to 0}\mathbf{H}_{\mathrm{obs}}^{\mathrm{F}} \times \lim_{s\to 0}(s\bar{\mathbf{V}}) + \lim_{s\to 0}\mathbf{H}_{\mathrm{NC}} \times \lim_{s\to 0}(s\mathbf{D}) = \mathbf{Q} \\ &\quad \times \lim_{t\to\infty}\mathbf{v} + \mathbf{0} = \mathbf{Q}\mathbf{v}^{\mathrm{ss}} = \langle \mathbf{v}^{\mathrm{ss}}\rangle\,\underline{\mathbf{1}}\end{aligned} \quad \text{(A.27)}$$

which proves the Theorem A.2. ■

APPENDIX III

MICROGRID PARAMETERS

Each of the underlying buck converters has $L = 2.64$ mH and $C = 2.2$ mF and works with the switching frequency of $F_s = 60$kHz. Transmission lines series impedances are $Z_{12} = Z_{34} = Z_b$ and $Z_{25} = Z_{35} = 2Z_b$, where the base impedance is $Z_b = 0.5 + (50\ \mu\mathrm{H}\ )s$. The circuit model of the line includes 22 nF of capacitance on either end. Impedances of the local loads are $R_1 = 30\ \Omega$ and $R_2 = R_3 = R_4 = 20\ \Omega$. Voltages of the (rectified) input dc sources are $V_{\mathrm{s}1} = V_{\mathrm{s}4} = 80$ V and $V_{\mathrm{s}2} = V_{\mathrm{s}3} = 100$ V. The control parameters are as follows:

$$\mathbf{I}_{\mathrm{rated}} = \mathrm{diag}\{6, 3, 3, 6\} \quad \text{(A.28)}$$

$$\mathbf{A_G} = \begin{bmatrix}0 & 90 & 0 & 110\\ 90 & 0 & 100 & 0\\ 0 & 100 & 0 & 120\\ 110 & 0 & 120 & 0\end{bmatrix}, \mathbf{r} = \begin{bmatrix}0.5 & 0 & 0 & 0\\ 0 & 1.0 & 0 & 0\\ 0 & 0 & 1.0 & 0\\ 0 & 0 & 0 & 0.5\end{bmatrix} \quad \text{(A.29)}$$

$$b = 1, c = 0.075 \quad \text{(A.30)}$$

$$\mathbf{H_P} = \begin{bmatrix}0.1 & 0 & 0 & 0\\ 0 & 0.09 & 0 & 0\\ 0 & 0 & 0.08 & 0\\ 0 & 0 & 0 & 0.11\end{bmatrix}, \mathbf{H_I} = \begin{bmatrix}6 & 0 & 0 & 0\\ 0 & 5 & 0 & 0\\ 0 & 0 & 5.4 & 0\\ 0 & 0 & 0 & 5.6\end{bmatrix} \quad \text{(A.31)}$$

$$\mathbf{G_P} = \begin{bmatrix}1.1 & 0 & 0 & 0\\ 0 & 1 & 0 & 0\\ 0 & 0 & 1.2 & 0\\ 0 & 0 & 0 & 1.1\end{bmatrix}, \mathbf{G_I} = \begin{bmatrix}7 & 0 & 0 & 0\\ 0 & 7.4 & 0 & 0\\ 0 & 0 & 6.6 & 0\\ 0 & 0 & 0 & 7\end{bmatrix} \quad \text{(A.32)}$$

$$\mathbf{K} = \begin{bmatrix}1 & 0 & 0 & 0\\ 0 & 2 & 0 & 0\\ 0 & 0 & 3 & 0\\ 0 & 0 & 0 & 4\end{bmatrix}. \quad \text{(A.33)}$$

REFERENCES

[1] J. M. Guerrero, J. C. Vasquez, J. Matas, L. G. de Vincuña, and M. Castilla, "Hierarchical control of droop-controlled AC and DC microgrids—A general approach toward standardization," *IEEE Trans. Ind. Electron.*, vol. 58, pp. 158–172, Jan. 2011.

[2] R. Majumder, B. Chaudhuri, A. Ghosh, R. Majumder, G. Ledwich, and F. Zare, "Improvement of stability and load sharing in an autonomous microgrid using supplementary droop control loop," *IEEE Trans. Power Syst.*, vol. 25, no. 2, pp. 796–808, May 2010.

[3] H. Kakigano, Y. Miura, and T. Ise, "Distribution voltage control for DC microgrids using fuzzy control and gain-scheduling technique," *IEEE Trans. Power Electron.*, vol. 28, no. 5, pp. 2246–2258, May 2013.

[4] H. Kakigano, Y. Miura, and T. Ise, "Low-voltage bipolar-type DC microgrid for super high quality distribution," *IEEE Trans. Power Electron.*, vol. 25, no. 12, pp. 3066–3075, Dec. 2010.

[5] Y. K. Chen, Y. C. Wu, C. C. Song, and Y. S. Chen, "Design and implementation of energy management system with fuzzy control for DC microgrid systems," *IEEE Trans. Power Electron.*, vol. 28, no. 4, pp. 1563–1570, Apr. 2013.

[6] D. Salomonsson, L. Söder, and A. Sannino, "An adaptive control system for a DC microgrid for data centers," *IEEE Trans. Ind. Appl.*, vol. 44, no. 6, pp. 1910–1917, Nov./Dec. 2008.

[7] A. Kwasinski, "Quantitative evaluation of DC microgrids availability: Effects of system architecture and converter topology design choices," *IEEE Trans. Power Electron.*, vol. 26, no. 3, pp. 835–851, Mar. 2011.

[8] Y. C. Chang and C. M. Liaw, "Establishment of a switched-reluctance generator-based common DC microgrid system," *IEEE Trans. Power Electron.*, vol. 26, no. 9, pp. 2512–2527, Sep. 2011.

[9] Y. Gu, X. Xiang, W. Li, and X. He, "Mode-adaptive decentralized control for renewable DC microgrid with enhanced reliability and flexibility," *IEEE Trans. Power Electron.*, vol. 29, no. 9, pp. 5072–5080, Sep. 2014.

[10] P. C. Loh, D. Li; Y. K. Chai, and F. Blaabjerg, "Autonomous operation of hybrid microgrid with AC and DC subgrids," *IEEE Trans. Power Electron.*, vol. 28, no. 5, pp. 2214–2223, May 2013.

[11] S. R. Huddy and J. D. Skufca, "Amplitude death solutions for stabilization of DC microgrids with instantaneous constant-power loads," *IEEE Trans. Power Electron.*, vol. 28, no. 1, pp. 247–253, Jan. 2013.

[12] N. Bottrell, M. Prodanovic, and T. C. Green, "Dynamic stability of a microgrid with an active load," *IEEE Trans. Power Electron.*, vol. 28, no. 11, pp. 5107–5119, Nov. 2013.

[13] D. Chen and L. Xu, "Autonomous DC voltage control of a DC microgrid with multiple slack terminals," *IEEE Trans. Power Syst.*, vol. 27, no. 4, pp. 1897–1905, Nov. 2012.

[14] M. Datta, T. Senjyu, A. Yona, T. Funabashi, and C. H. Kim, "A frequency-control approach by photovoltaic generator in a PV-diesel hybrid power system," *IEEE Trans. Energy Convers.*, vol. 26, no. 2, pp. 559–571, Jun. 2011.

[15] S. Teleke, M. E. Baran, A. Q. Huang, S. Bhattacharya, and L. Anderson, "Control strategies for battery energy storage for wind farm dispatching," *IEEE Trans. Energy Convers.*, vol. 24, no. 3, pp. 725–732, Sep. 2009.

[16] Z. Jiang and X. Yu, "Hybrid DC- and AC-linked microgrids: Towards integration of distributed energy resources," in *Proc. IEEE Conf. Global Sustain. Energy Infrastructure*, 2008, pp. 1–8.

[17] A. Kwasinski and C. N. Onwuchekwa, "Dynamic behavior and stabilization of DC microgrids with instantaneous constant-power loads," *IEEE Trans. Power Electron.*, vol. 26, no. 3, pp. 822–834, Mar. 2011.

[18] H. Ikebe, "Power systems for telecommunications in the IT age," in *Proc. IEEE 25th Int. Telecommun. Energy Conf.*, 2003, pp. 1–8.

[19] R. S. Balog, W. Weaver, and P. T. Krein, "The load as an energy asset in a distributed DC smartgrid architecture," *IEEE Trans. Smart Grid*, vol. 3, no. 1, pp. 253–260, Mar. 2012.

[20] L. Zhang, Y. Wang, H. Li, and P. Sun, "Hierarchical coordinated control of DC microgrid with wind turbines," in *Proc. IEEE 38th Annu. Conf. Ind. Electron. Soc.*, 2012, pp. 3547–3552.

[21] L. Xu and D. Chen, "Control and operation of a DC microgrid with variable generation and energy storage," *IEEE Trans. Power Del.*, vol. 26, no. 4, pp. 2513–2522, Oct. 2011.

[22] C. Yuen, A. Oudalov, and A. Timbus, "The provision of frequency control reserves from multiple microgrids," *IEEE Trans. Ind. Electron.*, vol. 58, no. 1, pp. 173–183, Jan. 2011.

[23] H. Kanchev, D. Lu, F. Colas, V. Lazarov, and B. Francois, "Energy management and operational planning of a microgrid with a PV-based active generator for smart grid applications," *IEEE Trans. Ind. Electron.*, vol. 58, no. 10, pp. 4583–4592, Oct. 2011.

[24] C. Chen, S. Duan, T. Cai, B. Liu, and G. Hu, "Optimal allocation and economic analysis of energy storage system in microgrids," *IEEE Trans. Power Electron.*, vol. 26, no. 10, pp. 2762–2773, Oct. 2011.

[25] T. Zhou and B. Francois, "Energy management and power control of a hybrid active wind generator for distributed power generation and grid integration," *IEEE Trans. Ind. Electron.*, vol. 58, no. 1, pp. 95–104, Jan. 2011.

[26] S. Anand, B. G. Fernandes, and J. M. Guerrero, "Distributed control to ensure proportional load sharing and improve voltage regulation in low-voltage DC microgrids," *IEEE Trans. Power Electron.*, vol. 28, no. 4, pp. 1900–1913, Apr. 2013.

[27] P. C. Loh, D. Li, Y. K. Chai, and F. Blaabjerg, "Autonomous control of interlinking converter with energy storage in hybrid AC–DC microgrid," *IEEE Trans. Ind. Appl.*, vol. 49, no. 3, pp. 1374–1382, May/Jun. 2013.

[28] J. Schönberger, R. Duke, and S. D. Round, "DC-bus signaling: A distributed control strategy for a hybrid renewable nanogrid," *IEEE Trans. Ind. Electron.*, vol. 53, no. 5, pp. 1453–1460, Oct. 2006.

[29] K. Sun, L. Zhang, Y. Xing, and J. M. Guerrero, "A distributed control strategy based on DC bus signaling for modular photovoltaic generation systems with battery energy storage," *IEEE Trans. Power Electron.*, vol. 26, no. 10, pp. 3032–3045, Oct. 2011.

[30] D. Chen, L. Xu, and L. Yao, "DC voltage variation based autonomous control of DC microgrids," *IEEE Trans. Power Del.*, vol. 28, no. 2, pp. 637–648, Apr. 2013.

[31] P. Karlsson and J. Svensson, "DC bus voltage control for a distributed power system," *IEEE Trans. Power Electron.*, vol. 18, no. 6, pp. 1405–1412, Nov. 2003.

[32] Y. Ito, Y. Zhongqing, and H. Akagi, "DC Microgrid based distribution power generation system," in *Proc. 4th Int. Power Electron. Motion Control Conf.*, 2004, pp. 1740–1745.

[33] W. Qiu and Z. Liang, "Practical design considerations of current sharing control for parallel VRM applications," in *Proc. 20th Annu. Appl. Power Electron. Conf. Expo.*, 2005, pp. 281–286.

[34] J. M. Guerrero, L. Hang, and J. Uceda, "Control of distributed uninterruptible power supply systems," *IEEE Trans. Ind. Electron.*, vol. 55, no. 8, pp. 2845–2859, Aug. 2008.

[35] X. Lu, K. Sun, J. M. Guerrero, J. C. Vasquez, and L. Huang, "State-of-charge balance using adaptive droop control for distributed energy storage systems in DC microgrid applications," *IEEE Trans. Ind. Electron.*, vol. 61, no. 6, pp. 2804–2815, Jun. 2014.

[36] R. A. F. Ferreira, H. A. C. Braga, A. A. Ferreira, and P. G. Barbosa, "Analysis of voltage droop control method for DC microgrids with simulink: Modeling and simulation," in *Proc. 10th IEEE/IAS Int. Conf. Ind. Appl.*, 2012, pp. 1–6.

[37] J. A. P. Lopes, C. L. Moreira, and A. G. Madureira, "Defining control strategies for microgrids islanded operation," *IEEE Trans. Power Syst.*, vol. 21, no. 2, pp. 916–924, May 2006.

[38] A. Tuladhar, H. Jin, T. Unger, and K. Mauch, "Control of parallel inverters in distributed AC power systems with consideration of line impedance effect," *IEEE Trans. Ind. Appl.*, vol. 36, no. 1, pp. 131–138, Jan./Feb. 2000.

[39] J. M. Guerrero, L. G. Vicuña, J. Matas, M. Castilla, and J. Miret, "Output impedance design of parallel-connected UPS inverters with wireless load sharing control," *IEEE Trans. Ind. Electron.*, vol. 52, no. 4, pp. 1126–1135, Aug. 2005.

[40] M. N. Marwali, J. W. Jung, and A. Keyhani, "Control of distributed generation systems—Part II: Load sharing control," *IEEE Trans. Power Electron.*, vol. 19, no. 6, pp. 1551–1561, Nov. 2004.

[41] K. De Brabandere, B. Bolsens, J. Van Den Keybus, A. Woyte, J. Driesen, and R. Belmans, "A voltage and frequency droop control method for parallel inverters," *IEEE Trans. Power Electron.*, vol. 22, no. 4, pp. 1107–1115, Jul. 2007.

[42] Y. Mohamed and E. F. El-Saadany, "Adaptive decentralized droop controller to preserve power sharing stability of paralleled inverters in distributed generation microgrids," *IEEE Trans. Power Electron.*, vol. 23, no. 6, pp. 2806–2816, Nov. 2008.

[43] X. Lu, J. M. Guerrero, K. Sun, and J. C. Vasquez, "An improved droop control method for DC microgrids based on low bandwidth communication with dc bus voltage restoration and enhanced current sharing accuracy," *IEEE Trans. Power Electron.*, vol. 29, no. 4, pp. 1800–1812, Apr. 2014.

[44] S. Anand and B. G. Fernandes, "Steady state performance analysis for load sharing in dc distributed generation system," in *Proc. 10th Int. Conf. Environ. Elect. Eng.*, 2011, pp. 1–4.

[45] Y. W. Li and C. N. Kao, "An accurate power control strategy for power-electronics-interfaced distributed generation units operation in a low voltage multi-bus microgrid," *IEEE Trans. Power Electron.*, vol. 24, no. 12, pp. 2977–2988, Dec. 2009.

[46] J. He and Y. W. Li, "Analysis, design and implementation of virtual impedance for power electronics interfaced distributed generation," *IEEE Trans. Ind. Appl.*, vol. 47, no. 6, pp. 2525–2538, Nov./Dec. 2011.

[47] W. Qiu and Z. Liang, "Practical design considerations of current sharing control for parallel VRM applications," in *Proc. 20th Annu. Appl. Power Electron. Conf. Expo.*, 2005, pp. 281–286.

[48] H. Laaksonen, P. Saari, and R. Komulainen, "Voltage and frequency control of inverter based weak LV network microgrid," in *Proc. Int. Conf. Future Power Syst.*, 2005, pp. 1–6.
[49] T. L. Vandoorn, B. Meersman, L. Degroote, B. Renders, and L. Vandevelde, "A control strategy for islanded Microgrids with DC-link voltage control," *IEEE Trans. Power Del.*, vol. 26, no. 2, pp. 703–713, Apr. 2011.
[50] L. Meng, T. Dragicevic, J. M. Guerrero, and J. C. Vasquez, "Optimization with system damping restoration for droop controlled DC–DC converters," in *Proc. IEEE Energy Convers. Cong. Expo.*, 2013, pp. 65–72.
[51] T. Dragicevic, J. M. Guerrero, J. C. Vasquez, and D. Skrlec, "Supervisory control of an adaptive-droop regulated DC microgrid with battery management capability," *IEEE Trans. Power Electron.*, vol. 29, no. 2, pp. 695–706, Feb. 2014.
[52] Q. Shafiee, J. M. Guerrero, and J. C. Vasquez, "Distributed secondary control for islanded Microgrids—A novel approach," *IEEE Trans. Power Electron.*, vol. 29, no. 2, pp. 1018–1031, Feb. 2014.
[53] V. Nasirian, A. Davoudi, and F. L. Lewis, "Distributed adaptive droop control for DC Microgrids," in *Proc. 29th IEEE Appl. Power Electron. Conf. Expo.*, 2014, pp. 1147–1152.
[54] R. Olfati-Saber and R. M. Murray, "Consensus problems in networks of agents with switching topology and time-delays," *IEEE Trans. Autom. Control*, vol. 49, no. 9, pp. 1520–1533, Sep. 2004.
[55] D. P. Spanos, R. Olfati-Saber, and R. M. Murray, "Dynamic consensus for mobile networks," in *Proc. 16th Int. Fed. Autom. Control*, 2005, pp. 1–6.
[56] M. Furukawa, J. Xu, Y. Shimizu, and Y. Kato, "Scratch-induced demagnetization of perpendicular magnetic disk," *IEEE Trans. Magn.*, vol. 44, no. 11, pp. 3633–3636, Nov. 2008.
[57] V. Sridharan, H. Asadi, M. B. Tahoori, and D. Kaeli, "Reducing data cache susceptibility to soft errors," *IEEE Trans. Dependable Secure Comput.*, vol. 3, no. 4, pp. 353–364, Oct./Dec. 2006.
[58] R. W. Erickson and D. Maksimovic, *Fundamental of Power Electronics*. 2nd ed., Norwell, MA, USA: Kluwer, 2001.
[59] V. Nasirian, Y. Karimi, A. Davoudi, M. R. Zolghadri, M. Ahmadian, and S. Moayedi, "Dynamic model development and variable switching-frequency control for DCVM Cúk converters in PFC applications," *IEEE Trans. Ind. Appl.*, vol. 49, no. 6, pp. 2636–2650, Nov./Dec. 2013.
[60] D. Nilsson and A. Sannino, "Efficiency analysis of low- and medium voltage DC distribution systems," in *Proc. IEEE Power Eng. Soc. Gen. Meet.*, 2004, pp. 2315–2321.
[61] S. Anand and B. G. Fernandes, "Optimal voltage level for DC Microgrids," in *Proc. IEEE 36th Annu. Conf. Ind. Electron. Soc.*, 2010, pp. 3034–3039.
[62] T. Pavlovic, T. Bjazic, and Z. Ban, "Simplified averaged models of DC–DC power converters suitable for controller design and microgrid simulation," *IEEE Trans. Power Electron.*, vol. 28, no. 7, pp. 3266–3275, Jul. 2013.
[63] Z. Qu, *Cooperative Control of Dynamical Systems: Applications to Autonomous Vehicles*. New York, NY, USA: Springer-Verlag, 2009.

Vahidreza Nasirian (S'12) received the B.S. and M.S. degrees in electrical engineering from Sharif University of Technology, Tehran, Iran, in 2007 and 2010, respectively. He is currently working toward the Ph.D. degree at the University of Texas at Arlington, Arlington, TX, USA.

He has received the Iranian National Elites Foundation fellowship for 2008–2010 and the Carrizo Oil & Gas Inc. Graduate Research fellowship for 2011–2013. His research interests include modeling and control of power electronics and electric drives, microgrid control, transportation electrification, and renewable and sustainable energy systems.

Mr. Nasirian received the gold medal in 20th National Mathematics Olympiad in 2002, Tehran, Iran, and the bronze medal in the Second Silk Road Mathematics Competition in 2003, Turkey.

Seyedali Moayedi (S'12) received the B.Sc. and M.Sc. degrees in electrical engineering from Sharif University of technology, Tehran, Iran, in 2007 and 2009, respectively. He is currently working toward the Ph.D. degree at the University of Texas at Arlington, Arlington, TX, USA.

His research interests include modeling and control of power electronics and electric drives, transportation electrification, and design and characterization of electromechanical energy converters.

Ali Davoudi (S'04–M'11) received B.Sc. and M.Sc. degrees in electrical and computer engineering from Sharif University of Technology, Tehran, Iran, and The University of British Columbia, Vancouver, Canada, in 2003 and 2005, respectively. He received the Ph.D. degree in electrical and computer engineering from the University of Illinois, Urbana-Champaign, IL, USA, in 2010.

He is currently an Assistant Professor at the Electrical Engineering Department, the University of Texas at Arlington, Arlington, TX, USA. He worked for Solar Bridge Technologies, Texas Instruments, Inc., and Royal Philips Electronics. His research interests include various aspects of modeling, simulation, and control of power electronics, energy conversion systems, and finite-inertia power systems.

Dr. Davoudi is an Associate Editor for IEEE TRANSACTIONS ON INDUSTRY APPLICATIONS.

Frank L. Lewis (F'94) received the bachelor's degree in physics/EE, and the M.S.E.E. degree from Rice University, Houston, TX, USA, the M.S. degree in aeronautical engineering from University of West Florida, Pensacola, FL, USA, and the Ph.D. degree from Georgia Tech, Atlanta, GA, USA.

He works in feedback control, reinforcement learning, intelligent systems, and distributed control systems. He is the author of 6 U.S. patents, 273 journal papers, 375 conference papers, 15 books, 44 chapters, and 11 journal special issues. He was a Distinguished Foreign Scholar, Nanjing University Science and Technology. He was also Project 111 Professor at Northeastern University, China.

Dr. Lewis received the Fulbright Research Award, NSF Research Initiation Grant, ASEE Terman Award, International Neural Network Society Gabor Award 2009, U.K. Institute Measurement and Control Honeywell Field Engineering Medal in 2009. He received IEEE Computational Intelligence Society Neural Networks Pioneer Award in 2012. He received Outstanding Service Award from Dallas IEEE section and was selected as an Engineer of the Year by Fort Worth IEEE Section. He was listed in Fort Worth Business Press Top 200 Leaders in Manufacturing. He received the 2010 IEEE Region 5 Outstanding Engineering Educator Award and the 2010 UTA Graduate Dean's Excellence in Doctoral Mentoring Award. He was elected to UTA Academy of Distinguished Teachers in 2012. He served on the NAE Committee on Space Station in 1995. He is the Founding Member of the Board of Governors of the Mediterranean Control Association. He helped win the IEEE Control Systems Society Best Chapter Award (as Founding Chairman of DFW Chapter), the National Sigma Xi Award for Outstanding Chapter (as President of UTA Chapter), and the U.S. SBA Tibbetts Award in 1996 (as the Director of ARRI's SBIR Program). He is a Member of the National Academy of Inventors, a Fellow IFAC, a Fellow U.K. Institute of Measurement and Control, PE Texas, and U.K. Chartered Engineer. He is also a UTA Distinguished Scholar Professor, a UTA Distinguished Teaching Professor, and the Moncrief-O'Donnell Chair at the University of Texas at Arlington Research Institute. He is also an IEEE Control Systems Society Distinguished Lecturer.